A Pulsed-Precipitation Model of Dryland Vegetation Pattern Formation*

Punit Gandhi[†], Lily Liu[‡], and Mary Silber[§]

Abstract. We develop a model for investigating the impact of rainstorm variability on the formation of banded vegetation patterns in dryland ecosystems. Water input, during rare rainstorms, is modeled as an instantaneous kick to the soil water. The redistribution, from surface water to soil moisture, accounts for the impact of vegetation on infiltration rate and downslope overland flow speed. These two positive feedbacks between water and biomass distributions act on the fast timescales of rain storms. During dry periods, a classic reaction-diffusion framework is used for the slow processes associated with soil water and biomass. This pulsed-precipitation model predicts that the preferred spacing of the vegetation bands is determined by the characteristic distance that a storm pulse of water travels overland before infiltrating into the soil. In this way, the vegetation pattern is determined by the fast ecohydrological processes and may be attuned with its dryland precipitation pattern. We demonstrate how this modeling framework, suited for stochastic rain inputs, can be used to investigate possible collapse of a dryland pattern-forming ecosystem under different precipitation patterns with identical low annual mean. Model simulations suggest, for instance, that shorter rainy seasons and greater variability in storm depth may both hasten ecosystem collapse.

Key words. pattern formation, dryland ecosystems, vegetation patterns, impulsive reaction-diffusion model, stochastic rainfall, ecosystem collapse

MSC codes. 35B36, 35R12, 35R60, 92D40, 86A05

DOI. 10.1137/22M1469572

1. Introduction. The availability of aerial photography in the 1940's first enabled the study of landscape-scale spatial patterns of vegetation growth in the Horn of Africa [30, 31]. On gentle slopes, $\lesssim 2\%$ grade, the patterns typically consist of bands of dense vegetation that are tens of meters wide and separated by bare soil (Figure 1). They exhibit regular spacing, with wavelength on the order of a hundred meters, and are oriented approximately perpendicular to the elevation grade. More recent studies incorporating modern satellite images have reported little change, relative to initial aerial photographs, at least in absence of increased human pressure [23]; the most remarkable change is a slow uphill migration of the pattern, on order of meters per decade [11]. It is now known that spontaneous formation of

^{*}Received by the editors January 6, 2022; accepted for publication (in revised form) by J. Rademacher October 4, 2022; published electronically May 19, 2023.

https://doi.org/10.1137/22M1469572

Funding: The work of the third author was supported in part by National Science Foundation grants DMS-1517416 and DMS-2023109.

^TDepartment of Mathematics and Applied Mathematics, Virginia Commonwealth University, Richmond, VA 23284 USA (gandhipr@vcu.edu).

[‡]University of Chicago, Chicago, IL 60637 USA (lilyliu14@gmail.com).

[§] Department of Statistics and the Committee on Computational and Applied Mathematics, University of Chicago, Chicago, IL 60637 USA (msilber@uchicago.edu).

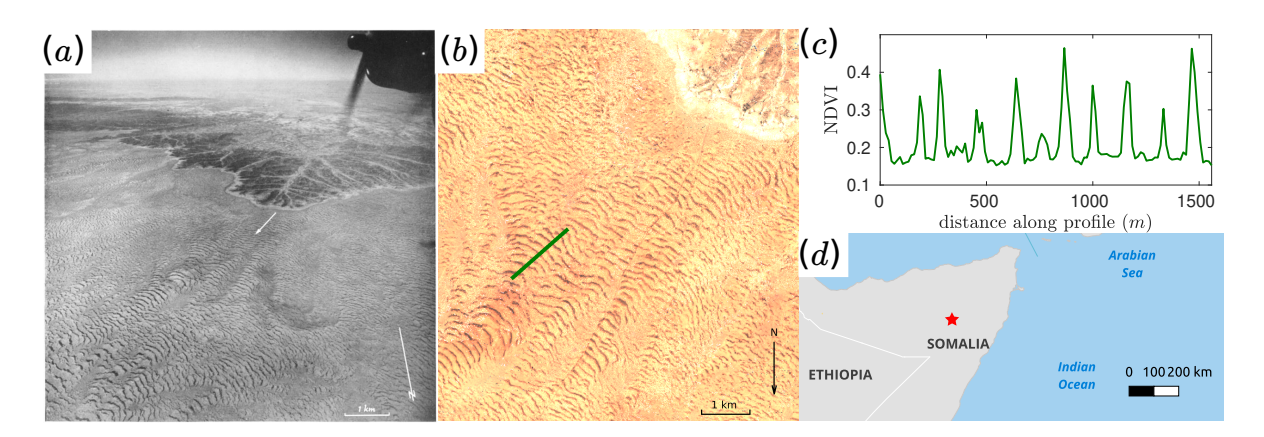


Figure 1. (a) Aerial photograph of banded vegetation patterns in the Sool region of Somalia, taken in March 1945 [23, 31]. (b) Satellite image of the same vegetation pattern taken in October 2020 from the Copernicus Sentinel 2 mission [14]. (c) Normalized difference vegetation index (NDVI) along the green line shown in panel (b). The location of the pattern (9°20'38" N 48°46'22" E) is indicated on the map in panel (d). [Used with permission of John Wiley and Sons, from [31]

periodic vegetation patterns occurs in drylands around the globe [10]. Mathematical models suggest that the phenomenon may be a strategy to exploit positive feedbacks that concentrate, in the vegetated zones, the limiting water resource [5, 19, 33].

The striking regularity of the dryland vegetation patterns has led to proposals that they may possess remotely sensed characteristics that are indicative of the ecosystem health and its risk of collapse [9, 39]. If true, monitoring changes in the patterns over time could provide information about the resilience of the ecosystems that support them, including their vulnerability under climate change. Many of the mathematical modeling studies have focused on pattern transitions, using mean annual precipitation level as a bifurcation parameter [21, 22, 24, 39, 49]. Indeed there is some observational evidence of significant changes in pattern morphology along an aridity gradient from South Sudan into Sudan [12]. Here we aim to expand the use of mathematical models to investigate changes in patterns, including possible collapse, under other characteristics of dryland precipitation, such as variability in storm frequency, storm depth, and length of rainy seasons.

Much of the currently available spatial remote sensing data provides information about the biomass distribution which, while fluctuating on a seasonal timescale, evolves on a decade timescale or longer. However, feedbacks between water and vegetation that are thought to be responsible for pattern formation involve a much faster rainstorm timescale. Detailed mechanistic models that attempt to bridge these disparate timescales can require significant computational resources to make useful predictions on the timescale of pattern evolution [17, 35]. Our approach to this challenge builds on a fast-slow switching framework [18] developed specifically to capture the processes involved, at a conceptual level, using the range of timescales on which they occur. We make some further simplifying assumptions about the fast processes that lead to a computationally tractable model for carrying out the large number of trials required to explore the impact of rainfall variability.

In contrast to the fast-slow switching model developed in [18], we do not attempt to resolve the short intra-rainstorm time in this current work, and instead treat each rain event as a Dirac-delta function impulse that deposits a uniform layer of water on the surface. We convert this surface water layer directly into an increase in the soil water distribution, taking into account the key feedbacks between the biomass distribution and (1) overland flow speed, and (2) infiltration rate. In analogy with "flow-kick" systems considered in the context of ecological resilience [34], the rain events become instantaneous "kicks" to the soil water in the reaction-diffusion model that governs the "flow," or time-evolution, of the ecosystem via water-biomass interactions. We use the resulting impulsive reaction-diffusion system [29] with nonlocal, spatially heterogeneous impulses to investigate vegetation bands on a one-dimensional hillslope with stochastic rainfall.

Many of the earliest conceptual PDE modeling efforts handle the multiple scales associated with vegetation pattern formation by formulating a model on an annually averaged timescale in which the fast processes are phenomenologically "upscaled" [21, 27, 38]. Mathematical analysis of such models that highlighted the mechanisms that set the spacing between vegetation bands or patches formulated this in terms of the wavenumber of Turing patterns in the context of reaction-diffusion models, or the analogous Turing-Hopf patterns when advection is also present [2, 43, 48]. A key feature of these models is that the wavenumber, and thus the predicted band or patch spacing, is controlled by the relative strengths of the transport terms, e.g. the phenomenological diffusion and advection constants incorporated into surface water, soil water, and biomass equations. Our analysis of the proposed pulsed-precipitation model has the characteristic band spacing set instead by the typical storm depth, which controls the distance that deposited surface water travels before it infiltrates into the soil. Moreover, the associated wavenumber is largely independent of the phenomenological diffusion constants incorporated into the soil water and biomass equations. In this way our results deviate from those of earlier conceptual models, and suggest interesting directions for future studies of more mechanistically detailed models and for field studies of the overland flow and infiltration that takes place after a storm, e.g., of the type reported in [6]. An interesting point of comparison can already be made between our wavenumber selection results and those presented in a recent paper by Crompton and Thompson [8]. Their study uses a different approach to determining the soil moisture distribution following a storm event. It is based on using machine learning to build an emulator for the Saint Venant shallow water equations for overland flow, coupled to the Richards equation for infiltration. They also find that greater storm depth, with identical annual mean, leads to increased spacing of the bands.

The impact of rainfall seasonality and variability on vegetation pattern dynamics is a major motivation for our study and has been explored in other works [13, 15, 25, 28, 45]. Here, we incorporate into the pulsed-precipitation model a stochastic rainfall that assumes a Poisson point process for storm arrivals and draws each storm depth from an exponential distribution [40]. We demonstrate how this model can be used to investigate the likelihood of noise-induced transitions between patterned states and barren desert states in a low annual-mean-rainfall, bistable regime. Specifically, we find that the vegetation can spontaneously collapse in a finite time as a result of fluctuations in rainfall and that both precipitation characteristics, such as the mean storm depth, and pattern characteristics, such as the band spacing, impact how long the vegetation survives on average. We find, for example, that greater variability in storm

depth increases the likelihood of collapse. The model also predicts that the same stochastic rainfall pattern, spread out over a longer rainy season, leads to longer-lived vegetation.

Our paper is organized as follows. In section 2, we summarize the fast-slow switching framework [18] that serves as a foundation for the pulsed-precipitation model used in this study, highlighting the key simplifications that make our stochastic rainfall simulations possible. In section 3, we leverage these simplifying assumptions to derive a pulsed-precipitation model in which rainstorms act as kicks to the soil moisture, which then evolves slowly, with the biomass, during the long dry periods between storms. In section 4, we investigate patternforming instabilities of spatially uniform states of the pulsed-precipitation model for an idealized periodic sequence of rain pulses. This linear stability analysis reveals a spatial resonance tongue structure that suggests the distance that surface water travels before infiltrating into the soil plays a key role in wavelength selection. In section 5, we numerically explore important qualitative differences in the dynamics of the model under stochastic rainfall versus periodic rainfall, while also showing that the wavelength, as in the linear problem, is tuned to mean overland flow distance of surface water following a storm. We then demonstrate how the model can be used to probe possible ecosystem collapse that results from rainfall variability in the bistable regime. Finally, in section 6, we discuss the results of our study in the context of other related work and suggest potential directions to pursue with the pulsed-precipitation model.

2. Fast-slow switching framework. This section introduces a model for the formation of banded vegetation patterns based on the fast-slow switching framework developed in [18]. The switching framework evolves, on appropriate timescales, three fields: surface water height H(X,T) [cm], soil water column height W(X,T) [cm], and biomass density B(X,T) [kg/m²]. While H(X,T) only evolves on the short timescale of rain events and B(X,T) only evolves on the long timescales between them, W(X,T) responds to processes that act on the fast timescale and other ones that occur on the slow timescale.

The output of the fast part of the switching model, after surface water has infiltrated the soil under an assumption of fixed biomass distribution $\mathcal{B}(X)$, is a soil moisture distribution $\mathcal{W}(X)$. This is the initial condition for the slow system that applies during the ensuing dry period between rain storms. The slow system evolves both biomass and soil moisture. It takes into account evapotranspiration of soil moisture, biomass growth and death, as well as seed dispersal, modeled as biomass diffusion, which leads to up-slope colonization of the vegetation. The explicit formulation of the fast and slow parts of the switching model are given in sections 2.1 and 2.2, respectively. We highlight the differences between the original formulation in [18] and the version used in this paper.

The modifications we introduce here allow for a closed form solution for the spatial distribution of soil water W once all of the surface water from a rainstorm has infiltrated into the soil. In section 3, we leverage this result to formulate a pulsed-precipitation model in which the biomass B(X,T) and soil water W(X,T) evolve on the slow timescale and rainstorms are treated as instantaneous impulses to W(X,T), determined by the closed form solution of the fast system, for a given storm depth and the current biomass profile.

Both the switching model and the pulsed-precipitation model are formulated on a onedimensional spatial domain with periodic boundary conditions; the perspective is that it is

Table 1

Comparison of infiltration rate \mathcal{I} and overland water flow speed \mathcal{V} used with the fast-slow switching model in [18] and our modified pulsed-precipitation model. For the pulsed-precipitation model, we set $K_I = 200\,\mathrm{cm/day}$, whereas for the fast-slow model we used $\overline{K}_I = 500\,\mathrm{cm/day}$ with $A = 1\,\mathrm{cm}$, $W_s = 27\,\mathrm{cm}$, and $\beta_I = 4$ for the additional factors that can reduce infiltration. Both $\beta_V = 2/3$ (with $K_V \sqrt{\zeta} = 1.4\,\mathrm{m/day/cm^{2/3}}$) and the computationally faster $\beta_V = 0$ (with $K_V \sqrt{\zeta} = 1.4\,\mathrm{m/day}$) were used in [18]. All other parameters match values for the pulsed-precipitation model given in Table 2. Here $\Theta(H)$ denotes a Heaviside step function in H.

	Fast-slow [18]	Pulsed-precipitation
Infiltration rate	$\overline{K}_I \left(\frac{\mathcal{B}(X) + fQ}{\mathcal{B}(X) + Q} \right) \left(\frac{H}{H + A} \right) \left(1 - \frac{W}{W_s} \right)^{\beta_I}$	$K_I\left(\frac{\mathcal{B}(X)+fQ}{\mathcal{B}(X)+Q}\right)\Theta(H)$
Surface flow speed	$\left(rac{K_V\sqrt{\zeta}}{1+N\mathcal{B}(X)} ight)\!H^{eta_V}$	$rac{K_V\sqrt{\zeta}}{1+N\mathcal{B}(X)}$

capturing some representative middle portion of a long swath of gently sloped terrain, oriented with uphill in the +X direction. We conclude in section 2.3 by presenting the rainfall models used in this study, inspired by a typical climatology in the Horn of Africa.

2.1. Fast subsystem of the switching model. The fast portion of the switching model is

(2.1a)
$$\frac{\partial H}{\partial T} = \underbrace{P(T)}_{Precip.} - \underbrace{\mathcal{I}\Big(H,W;\mathcal{B}(X)\Big)}_{Infiltration} + \underbrace{\frac{\partial}{\partial X}\Big(\mathcal{V}(H;\mathcal{B}(X))\ H\Big)}_{Advection},$$

(2.1b)
$$\frac{\partial W}{\partial T} = \underbrace{\mathcal{I}\Big(H, W; \mathcal{B}(X)\Big)}_{Infiltration},$$

where the infiltration rate, \mathcal{I} [cm/day], and overland surface flow speed, \mathcal{V} [m/day], are given in Table 1 for both the original fast slow model and the approximation that leads to the pulsed-precipitation model.

In the pulsed model, the H and W dependent factors in \mathcal{I} are replaced by a Heaviside step function in H; infiltration occurs whenever there is water on the surface at a rate that depends only on \mathcal{B} at that location. With the default value of f = 0.1, the bare soil infiltration rate ($\mathcal{B} = 0 \text{ kg/m}^2$) is a factor of 10 slower than its maximum rate for $\mathcal{B} \gg Q$. This sigmoidal transition from low to high infiltration rate with increasing biomass \mathcal{B} is an essential positive feedback and suggests an advantage for \mathcal{B} to exceed the threshold Q in its patterned state.

We assume a constant 0.5% elevation grade ($\zeta = 0.005$) and, as is common in conceptual models for vegetation pattern formation, we omit the dependence on H in the speed of overland flow \mathcal{V} for the pulsed-precipitation model. We note that exactly what dependence is most appropriate in this setting is still an open question, and the impact on qualitative predictions may potentially be minimized by appropriately calibrating the model [7]. The overland flow speed is decreased, by a factor $1 + N\mathcal{B}(X)$, if there is vegetation at a location X. This longer residence time, of surface water on vegetated soil compared to bare soil, is another positive feedback between water resource and biomass that acts on the fast timescale.

2.2. Slow subsystem of the switching model. The slow portion of the switching model evolves the soil water W(X,T), initialized by its post-storm distribution W(X), and the biomass density B(X,T). Specifically,

(2.2a)
$$\frac{\partial W}{\partial T} = -\underbrace{\left(L + \Gamma B\right)W}_{Evapotranspiration} + \underbrace{D_W \frac{\partial^2 W}{\partial X^2}}_{Diffusion},$$

(2.2b)
$$\frac{\partial B}{\partial T} = \underbrace{C\left(1 - \frac{B}{K_B}\right)\Gamma BW}_{Growth} - \underbrace{MB}_{Death} + \underbrace{D_B \frac{\partial^2 B}{\partial X^2}}_{Dispersal}.$$

Here, the evaporation rate is given by L and the transpiration rate is given by ΓB . Transpiration dictates the biomass growth rate with an efficiency set by the parameter C and with a logistic term that limits growth if B approaches a carrying capacity K_B . The death rate M is constant, and seed dispersal is modeled by linear diffusion. As is done in [18], we typically neglect the soil water diffusion, i.e., $D_W = 0$. Our simulation results with $D_W > 0$ indicate that soil water diffusion plays a negligible role in the model. See Appendix A for numerical exploration of the impact of diffusion rates D_B and D_W on pattern formation within the pulsed-precipitation model.

2.3. Precipitation model. We use rainfall patterns in the Horn of Africa as inspiration for our rainfall models. Figure 2(a–d) shows rainfall statistics, based on reanalysis data of rainfall rates [26] at the site shown in Figure 1, between 2015 and 2020, along with associated cumulative rainfall.

Rainfall statistics in Figure 2(a–c), which are based on rainfall rates shown in Figure 2(d), indicate two rain seasons per year, each lasting approximately 1–2 months with annual precipitation fluctuating between 11 and 25 cm/year over the 5-year period. We emphasize that the data presented in Figure 2, while corrected using available rain gauge data, is reanalysis data based on models and not directly measured. We can therefore reliably report rainfall rate statistics, but not rainstorm depth statistics, which would be most relevant for informing the pulsed-precipitation model.

Investigations in [18], with the fast-slow switching model, collapsed the rainfall of each rainy season into a single hours-long storm of constant intensity, as illustrated in Figure 2(e). The pulsed-precipitation model, introduced in section 3, assumes each rainstorm instantaneously deposits water on the surface. We note that this is an assumption of convenience, and other studies have explored the role that storm duration can play in vegetation patterns [8]. In Appendix B, we show how we might capture the effects of storm duration in the pulsed-precipitation model by interpreting the storm depth as an effective surface water height during a storm.

In order to carry out linear stability analysis in section 4, we consider a periodic array of identical, evenly spaced rain pulses within each rainy season, as illustrated in Figure 2(f). In section 5 we explore the dynamics under a stochastic rainfall model [40] that treats rainstorm arrivals as a Poisson point process, during each fixed duration rainy season, with storm depths drawn from an exponential distribution, as illustrated in Figure 2(g).

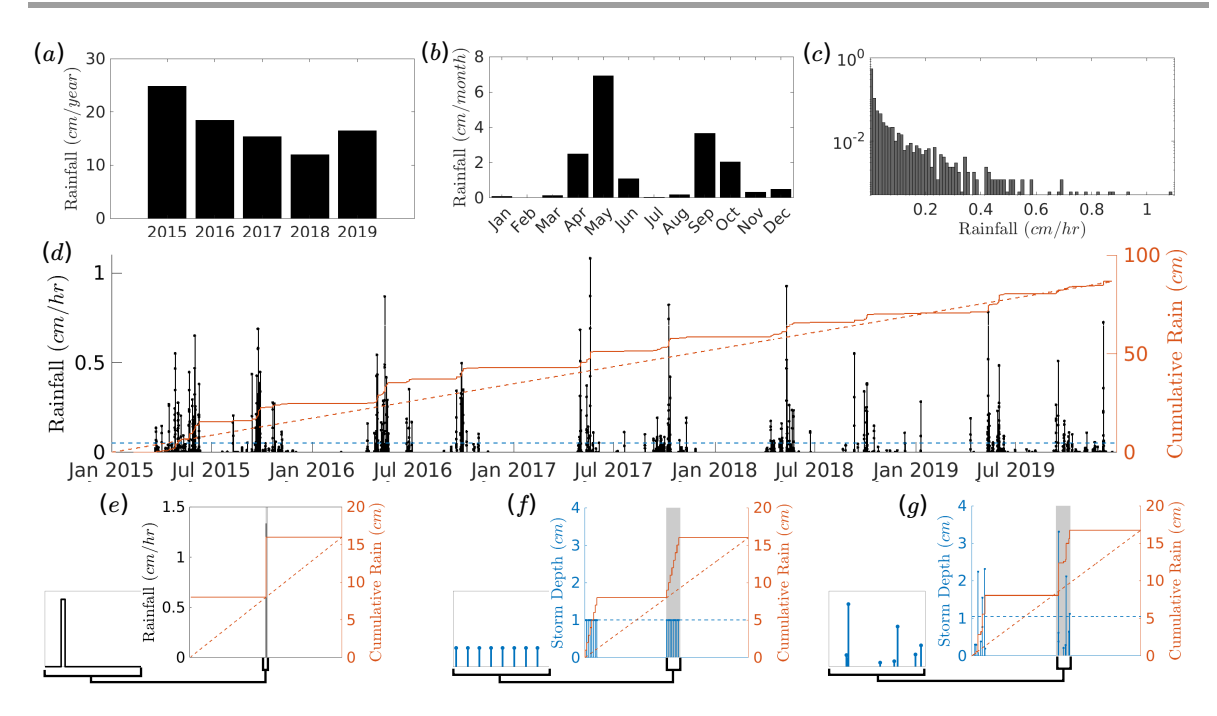


Figure 2. (a) Annual totals, (b) average monthly totals, and (c) rainfall rate distribution for (d) five years of half-hourly reanalysis rainfall data [26] at the location from Figure 1(d). Also shown is the time series generated by (e) the periodic rainfall model used in [18], consisting of a six-hour storm with a storm depth of 8 cm, repeating every six months, (f) the periodic rainfall model with eight instantaneous pulses with storm depth of 1 cm, evenly spaced in each one-month biannual rainy season, and (g) the stochastic rainfall model with two one-month rainy seasons per year, mean storm depth of 1 cm, and mean annual precipitation of 16 cm. Note that rainfall in the pulsed precipitation model is characterized by storm depth in cm (blue), whereas the rainfall in the fast-slow model is given in terms of a rainfall rate cm/hr over a given interval of time (black).

- **3. Pulsed-precipitation model.** This section develops the model we use in this paper for stochastic precipitation simulations. While we retain the same reaction-diffusion model (2.2) for the slow subsystem, we make two significant changes to the fast subsystem (2.1), which allow us to determine its output soil moisture distribution $\mathcal{W}(X)$ in a closed form, by quadrature. The model changes are the following:
 - 1. The precipitation P(T) in (2.1a) is replaced by rain events that instantaneously deposit a column of water, of height H_0 , uniformly on the domain. The timing and strength of these "precipitation pulses" are the random variables in our stochastic simulations.
 - 2. The infiltration rate used in [18], given in Table 1, is replaced by

(3.1)
$$\mathcal{I}(H;\mathcal{B}(X)) \equiv K_I \left(\frac{\mathcal{B}(X) + fQ}{\mathcal{B}(X) + Q}\right) \Theta(H).$$

The infiltration is independent of how saturated the soil might be and has a simple on-off switch with presence-absence of surface water. We model this with the Heaviside unit step function $\Theta(H)$, assuming the convention that $\Theta(0) = 0$.

With these modifications we are able to reformulate the fast-slow model into a pulsed-precipitation framework, with rain input modeled by instantaneous kicks to the soil water

followed by evolution of the slow system during the intervening dry-surface time intervals. We compare results from the two models in Appendix B.

The nondimensionalization in section 3.1 reveals key characteristic scales associated with the modified fast and slow subsystems (2.1)–(2.2). In section 3.2, we solve the fast system to obtain the spatial distribution of water that has infiltrated the soil following a Dirac-delta rain impulse. Algebraic manipulation of the integral expression for the soil water kick provides a geometric interpretation of the infiltration process that redistributes water from the surface into the soil.

3.1. Dimensionless parameters. In this subsection we present the dimensionless version of the pulsed precipitation model used in our investigations. For this, we introduce two different (dimensionless) timescales, t and τ for the fast and slow subsystems, respectively, and a dimensionless distance x. Specifically, we let

(3.2)
$$t = \frac{K_I}{\mathcal{H}_0} T, \quad \tau = MT, \quad x = \frac{K_I/\mathcal{H}_0}{K_V \sqrt{\zeta}} X.$$

Here, \mathcal{H}_0 is a characteristic rain pulse height and \mathcal{H}_0/K_I is an associated infiltration timescale. This time, together with a characteristic overland flow speed $(K_V\sqrt{\zeta})$, determines a characteristic overland travel distance $(\mathcal{H}_0/K_I)/(K_V\sqrt{\zeta})$ that is used to nondimensionalize X. We set the (slow) biomass timescale by its mortality rate, M. Finally, we define the dimensionless fields:

(3.3)
$$h = \frac{H}{\mathcal{H}_0}, \quad w = \left(\frac{C\Gamma}{M}\right)W, \quad b = \frac{B}{Q}.$$

The fast subsystem of the pulsed-precipitation model, in dimensionless variables, is

(3.4a)
$$\frac{\partial h}{\partial t} = -\iota(x)\Theta(h) + \frac{\partial}{\partial x}(\nu(x)h),$$

(3.4b)
$$\frac{\partial w}{\partial t} = \alpha \iota(x)\Theta(h),$$

where

(3.5)
$$\iota(x) = \frac{\hat{b}(x) + f}{\hat{b}(x) + 1}, \quad \nu(x) = \frac{1}{1 + \eta \hat{b}(x)}.$$

Because the rainstorm is assumed to deposit water on the surface instantaneously, we take $h = h_0$ as the initial condition for (3.4a), and there is no longer an explicit precipitation term. The dimensionless biomass distribution $\hat{b}(x) \equiv \mathcal{B}(X)/Q$ is taken from the slow subsystem at the arrival time of the precipitation pulse. The nondimensionalized slow subsystem is

(3.6a)
$$\frac{\partial w}{\partial \tau} = \delta_w \frac{\partial^2 w}{\partial x^2} - (\sigma + \gamma b)w,$$

(3.6b)
$$\frac{\partial b}{\partial \tau} = \delta_b \frac{\partial^2 b}{\partial x^2} + wb \left(1 - \frac{b}{\kappa} \right) - b.$$

Table 2

Summary of parameters used in numerical simulations. Values are given for the dimensioned fast-slow model (2.1)–(2.2) and the nondimensionalized pulsed precipitation model (3.4)–(3.6). We neglect soil water diffusion so $\delta_w = 0$.

Parameter	Units	Default value	Description/definition
$\overline{\mathcal{H}_0}$	cm	1	Characteristic precipitation pulse
K_I	cm/day	200	Infiltration rate coefficient
f	_	0.1	Bare/vegetated infiltration contrast
Q	kg/m^2	0.1	Biomass level for infiltration enhancement
$K_V\sqrt{\zeta}$	m/day	1.4×10^{4}	Surface water speed (bare soil)
N	m ² /kg	20	Surface roughness coefficient
L	day^{-1}	0.0075	Evaporation rate
Γ	$(kg/m^2)^{-1}day^{-1}$	0.025	Transpiration coefficient
K_B	kg/m^2	4	Biomass carrying capacity
C	$(kg/m^2)/cm$	0.1	Water use efficiency coefficient
M	day^{-1}	0.01	Biomass mortality rate
D_B	m^2/day	0.01	Biomass diffusion
D_W	m^2/day	0	Soil water diffusion
η	=	2	$\eta \equiv NQ$
α	_	0.25	$\alpha \equiv \mathcal{H}_0 C\Gamma/M$
σ	=	0.75	$\sigma \equiv L/M$
γ	=	0.25	$\gamma \equiv \Gamma Q/M$
κ	=	40	$\kappa \equiv K_B/Q$
δ_w	=	0	$\delta_w \equiv D_W K_I^2 / (M \mathcal{H}_0^2 K_V^2 \zeta)$
δ_b	_	0.0002	$\delta_b \equiv D_B K_I^2 / (M \mathcal{H}_0^2 K_V^2 \zeta)$

Definitions of the dimensionless parameters, and typical values used in simulations for all dimensioned parameters of the model, are given in Table 2; see [18] for details of these parameter estimates. Note that for the default parameters the fast infiltration timescale in (3.2) is less than 10 minutes, while the slow time-scale associated with the biomass is 100 days. The characteristic distance for overland water flow is $\sim 70\,\mathrm{m}$. This contrasts with the short biomass diffusion scale of $2\sqrt{365D_B}\approx 2.4\,\mathrm{m}$, which is based on a year timespan. The disparity of these two lengthscales is reflected in the nondimensionalized model through small diffusion parameter $\delta_b \ll 1$. Finally, we note that the characteristic soil water depth in (3.3) is $W_0 = M/C\Gamma = 4cm = 4\mathcal{H}_0$.

3.2. Solving the fast subsystem of the pulsed-precipitation model. The goal of this subsection is to obtain a closed form expression for $\widehat{w}(x)$, which is the amount of soil water at each location x, after the rain event. This distribution, together with $\widehat{b}(x)$, is then the initial condition for the slow subsystem (3.6) that applies during the ensuing dry spell. Before going into the details of the calculation, we present a schematic summary of the result in Figure 3. In particular, this figure illustrates the redistribution and infiltration processes that determine the amount of water from the rain event that infiltrates into a given location. The biomass level is indicated with high (low) levels shaded in green (yellow) in the upper part of both panels. The left panel illustrates the initial surface water input by the blue (and red) shaded region below some initial surface water height h_0 in the positive (x, h) quadrant. This initial amount of water is redistributed by downhill surface transport and infiltration, resulting in

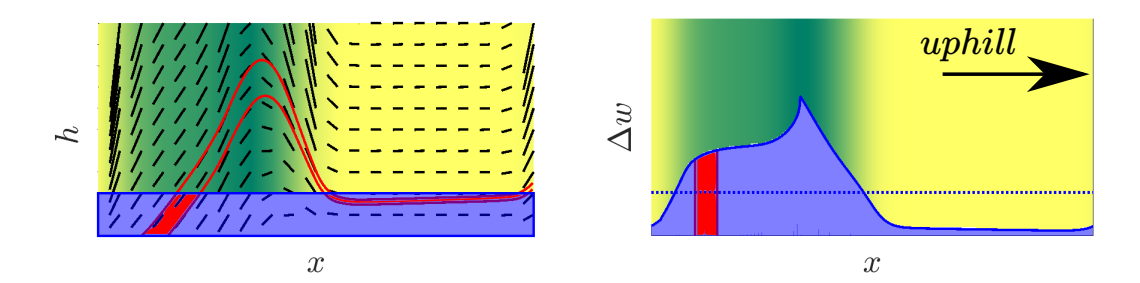


Figure 3. Illustration of the surface water transport and infiltration process modeled by the fast system (3.4). The initial surface water, shaded blue and red in the left panel, is redistributed by the dynamics of the fast system to a soil water distribution indicated by the corresponding shaded regions in the right panel. The spatial biomass profile is indicated with high/low levels in green/yellow in the upper portions of both panels. The direction field associated with the characteristic equation (3.7) is indicated in black in the left panel, with two example curves in red. The red region between the two example curves, constrained to be below the initial height h_0 , determines the soil water in red in the right panel. As indicated by the arrow in the right panel, x increases in the uphill direction.

the soil water distribution indicated by the blue (and red) shaded region in the right panel. Specifically, the amount of the initial block of surface water between the two red curves in the left panel, filled in red, infiltrates the soil at the locations where those curves reach h = 0. This contribution to soil moisture is summarized by the corresponding red block in the right panel. Note that the added soil water distribution Δw , shown in the right panel, is concentrated where the biomass is located, reflecting the positive feedbacks of the system.

In this section, we describe how we obtain the red curves that define the redistribution process as the solution of system (3.4) by a standard application of the method of characteristics (see, e.g., [16]). In particular, the solutions to the h equation (3.4a) along so-called characteristic curves, defined below by (3.8), partition the initial water by where it ends up in the soil, as illustrated in Figure 3. Figure 4 provides further details behind our approach for the biomass profile, $\mathcal{B}(X) \equiv Q\hat{b}(x)$, shown in panel (c). It fills in the steps to our geometric interpretation (Figure 3) for the way water, initialized on the surface, gets redistributed into the soil. While the following discussion of our method assumes an infinite domain to make the presentation of the underlying ideas more clear, our simulations incorporate periodic boundary conditions on a domain of length L.

We employ the method of characteristics to solve the fast subsystem (3.4), given a biomass distribution $\hat{b}(x)$, which determines the infiltration rate $\iota(x)$ and overland flow speed $\nu(x)$ via (3.5). We assume that the initial surface water height is $h(x,0) = h_0$, which is set by the precipitation pulse, and that the initial soil water distribution is $w(x,0) = w_0(x)$. We begin with the h equation (3.4a), which is decoupled from the w equation (3.4b) thanks to our simplifying assumptions related to the infiltration function \mathcal{I} . We parameterize time t(x;y) by spatial position x along a characteristic that starts at x = y at time t = 0. This results in the following set of ODEs, one for each $\hat{h}(x;y) \equiv h(x,t(x;y))$, the height of the surface water along the characteristic starting at y:

$$(3.7) \qquad \qquad \frac{d}{dx} \Big(\nu(x) \hat{h}(x;y) \Big) = \iota(x) \Theta\Big(\hat{h}(x;y) \Big), \quad \hat{h}(y;y) = h_0,$$

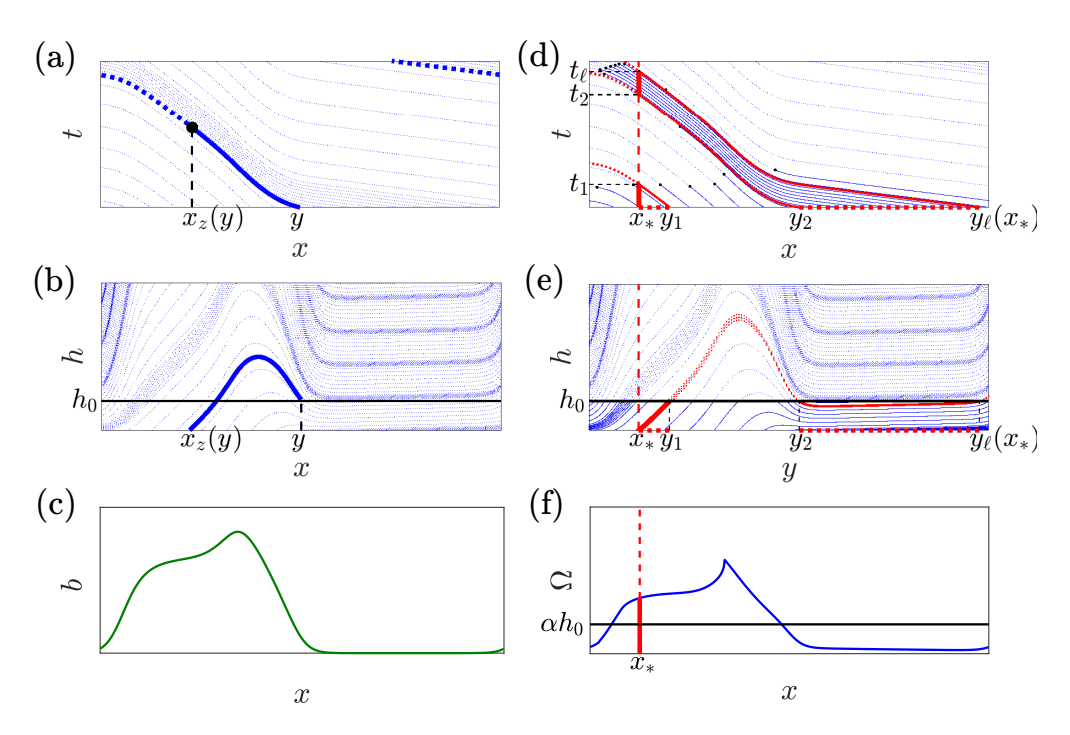


Figure 4. (a) The space time characteristic, defined by (3.8), with initial condition $h(y,0) = h_0$ is highlighted in bold. Surface water h reaches zero at $x_z(y)$ along the characteristic, which is indicated by a transition from solid to dotted line. (b) The corresponding picture in the (x,h) plane shows how h evolves along the characteristic, labeled by the location y of the initial height h_0 . (c) The biomass profile is included to highlight its role of slowing water flow and increasing infiltration. (d) The space time characteristics for which h reaches zero at $x = x_*$ are highlighted in red. The (vertical) time intervals $(0, t_1)$ and (t_2, t_ℓ) at $x = x_*$ capture the times for which h > 0 at $x = x_*$ and infiltration occurs. (e) The corresponding picture in the (y, h) plane indicates that the contributions to the soil water at $x = x_*$ come from locations with $h < h_0$ along the characteristic labeled by $y = y_\ell(x_*)$ which, by definition (3.12), reaches h = 0 at x_* . (f) The contribution from the rainstorm to the soil water at $x = x_*$, determined by (3.13), is highlighted in red.

where the time to reach the position $x \leq y$ along the characteristic starting at y is given by

(3.8)
$$t(x;y) = \int_{x}^{y} \frac{1}{\nu(s)} ds.$$

Based on the functional forms, we can assume $\nu(x)$ and $\iota(x)$ are continuous and strictly positive. Therefore, by (3.7), the product $q(x;y) = \nu(x)\hat{h}(x;y)$, which is initially positive at x = y, decreases monotonically as x decreases, i.e., in the downhill direction. It can reach zero only when $\hat{h}(x;y) = 0$, and for x values below this point, $\hat{h}(x;y)$ remains zero, a consequence of the Heaviside function in (3.7). For the characteristic starting at y, we denote that point where the surface water reaches zero by $x_z(y)$. We can then integrate (3.7) from the start of the characteristic y to some point x to get

(3.9)
$$\hat{h}(x;y) \equiv h(x,t(x,y)) = \begin{cases} \frac{1}{\nu(x)} \left(\nu(y)h_0 - \int_x^y \iota(s)ds \right) & \text{if } x_z(y) < x \le y, \\ 0 & \text{if } x \le x_z(y). \end{cases}$$

Figure 4(a) illustrates a number of characteristics t(x;y) satisfying (3.7). (Note that due to the periodic boundary conditions the characteristics wrap around the domain.) We indicate the point on the characteristic where $\hat{h}(x;y)$ first reaches zero, $(x_z(y), t(x_z(y);y))$, by a black circle and change to a dotted line where $\hat{h}(x;y) = 0$.

With a solution for h in hand, we now turn to the soil water equation (3.4b). We can write a formal solution for $\widehat{w}(x)$ in terms of h(x,t) as

(3.10)
$$\widehat{w}(x) = w_0(x) + \underbrace{\alpha \iota(x) \int_0^\infty \Theta(h(x,t)) dt}_{\equiv \Omega(x), \text{ added soil water}}.$$

Here, the integral over the Heaviside function determines the total length of time surface water is infiltrating the soil after a rain pulse on the fast timescale. Figure 4(d) indicates, with thick red vertical line segments, two intervals that comprise this time for the given point $x = x_*$. In order to compute the integral in (3.10) given our solution $\hat{h}(x;y)$ in (3.9), we make the change of variables from time t to the starting position y of the characteristic that reaches x at time t(x;y) via (3.8). The added soil water is given by

(3.11)
$$\Omega(x) = \alpha \iota(x) \int_{x}^{\infty} \frac{\Theta(\hat{h}(x;y))}{\nu(y)} dy.$$

The positive contributions to the integral in (3.11) occur for values of y where the surface water height h is nonzero at x along the characteristic starting at y. There are two such intervals in y associated with $x = x_*$ for the example in Figure 4(d), which are indicated with thick dotted red lines along the spatial axis. The characteristics highlighted in red in Figure 4(d) have surface water height that just reaches 0 at $x = x_*$ and mark the boundaries of the contributing intervals for (3.10) and (3.11). Figure 4(f) shows the resulting soil water distribution $\Omega(x)$ added by the impulse of rain. The contribution at $x = x_*$ highlighted by a thick solid red line is proportional to the time during which infiltration occurs.

In order to develop a geometric interpretation of (3.11), we return to our set of ODEs for $\hat{h}(x;y)$, with each labeled by y and given in (3.7). Notice that it is possible for multiple characteristics to first reach zero surface water height at the same location, that is, $x_z(y_1) = x_z(y_2)$ for $y_1 \neq y_2$. Because we assume the surface water is initially uniformly distributed across the entire domain, there is at least one characteristic that first reaches zero at any point x on the domain. We define $y_\ell(x)$ to be the largest y such that $x_z(y) = x$. Now, integrating (3.7), along this $y_\ell(x)$ characteristic, from x where the surface water reaches zero up to some point $y < y_\ell(x)$ gives

(3.12)
$$\hat{h}(y; y_{\ell}(x)) = \frac{1}{\nu(y)} \int_{x}^{y} \iota(s) ds.$$

The integral in (3.12) represents the height of the surface water at a point y along a characteristic defined by (3.7) and (3.8) that starts at x with h = 0 and follows it backward in time. We use the same notation \hat{h} as in (3.9) here because the result of the integral in (3.12) is equivalent to the surface water height at the point y along the same characteristic curve, but starting at $y_{\ell}(x)$ with $h = h_0$ and integrating forwards in time.

Noting that a positive multiplicative factor $\nu(x)/\nu(y)$ can be inserted in the argument of the Heaviside step function of (3.7), we can make use of (3.9) together with (3.12) to re-express the added soil water $\Omega(x)$ as

(3.13)
$$\Omega(x) = \alpha \iota(x) \int_{x}^{y_{\ell}(x)} \frac{\Theta\left(h_{0} - \hat{h}(y; y_{\ell}(x))\right)}{\nu(y)} dy.$$

We can truncate the upper bound of the integral in going from (3.11) to (3.13) because we have defined $y_{\ell}(x)$ such that $\hat{h}(y; y_{\ell}(x)) > h_0$ for all $y > y_{\ell}(x)$.

Equation (3.13) affords a geometric picture for the water going from the surface into the soil. We imagine beginning with a "block" of water on the surface as a result of the rainstorm, which is represented by the region between the thick solid black line and the y-axis in the (y,h)-plane in Figure 4(e). The fast system acts to redistribute this initial block of water into the soil via surface transport and infiltration. We can think of the characteristics defined by (3.12) that start at h=0 and move backward in time as a partitioning of this block in the (y,h)-plane. The amount of the initial block of water that appears along a characteristic, starting at a location x with h=0, is how much water infiltrates into that location. Notice that the contribution to $\Omega(x)$ along a characteristic is limited by the Heaviside function to intervals where $h < h_0$, e.g., within the initial block of water. Typical characteristics are indicated in Figure 4(e) by blue lines, with the intervals above h_0 dotted. The characteristic that starts at $x = x_*$ and determines the amount of added soil water at that location is highlighted in red. Notice that there are two intervals of this characteristic below h_0 . The endpoints of these segments correspond exactly to the endpoints of the intervals of integration (x_*, y_1) and $(y_2, y_\ell(x_*))$ shown in Figure 4(d). Indeed, all the characteristics that start with $h = h_0$ at t = 0 and reach zero at $x = x_*$ in the (x,t)-plane of Figure 4(d) map onto segments of the characteristic that starts with h=0 at $x=x_*$ in the (y,h)-plane of Figure 4(e).

The numerical simulations reported on in sections 4 and 5 are carried out using the ODE suite of MATLAB [42]. The contribution to the soil water from each rain pulse is computed by numerical integration of (3.12)–(3.13) via the trapezoidal rule. A centered finite-difference scheme is used to evolve the slow system (3.6) in between the rain pulses.

4. Periodic rainfall. We begin exploration of the pulsed-precipitation model by first considering an evenly spaced sequence of identical rain events within each rainy season, which is the periodic case shown in Figure 2(f). We find that the regularity of this artificial rainfall pattern leads to a spatial resonance phenomenon that controls the preferred spacing of the vegetation bands. Specifically, the spacing is determined by the distance surface water can travel in the time it takes for the precipitation pulse to fully infiltrate into the soil. We show this explicitly in section 4.1 through a linear stability analysis of the uniform vegetation state to spatially periodic perturbations proportional to e^{ikx} . This analysis reveals a sequence of resonance tongues in a (\mathcal{MAP}, k) -parameter plane, where \mathcal{MAP} denotes mean annual precipitation. We then use this insight to understand the preferred spacing and travel direction of the fully nonlinear bands, which is obtained through numerical simulations of the model in section 4.2.

Throughout this section we use a precipitation model consisting of $N_s = 2$ identical rainy seasons, six months apart, so the periodicity is $T_p = (365/2)$ days. Each rainy season lasts for

a time $T_r = (365/12) \,\mathrm{days} \equiv 1 \,\mathrm{month}$, and it consists of N_p equally spaced rain pulses that deliver, instantaneously, a column of water of height H_0 . The mean annual precipitation is then $\mathcal{MAP} = N_s N_p H_0$. We denote dimensionless time units by τ , with the six-month period of the seasonal forcing given by $\tau_p = 1.825$, and the month-long rainy season lasting a time $\tau_r = \tau_p/6$. The precipitation pulses, in dimensionless units, are denoted by h_0 .

4.1. Linear stability of spatially uniform, temporally periodic solutions. In this subsection, we describe results of linear stability computations for uniform vegetation to heterogeneous perturbations, proportional to e^{ikx} . The uniform state has the same half-year periodicity as the rainfall pattern and is determined as a fixed point of an appropriate stroboscopic map. Its linear stability properties are determined by a computation of Floquet multipliers as a function of k.

Loss of stability of bare soil solution. We find that the uniform vegetation state arises from a transcritical bifurcation of the zero-biomass desert state at $\mathcal{MAP} = \mathcal{MAP}_c \equiv LM/C\Gamma$. In particular, as shown in Appendix C, this threshold is independent of the details of the rainfall model. In fact, if we were to replace our fast-slow system for the uniform solutions by a pair of ODEs for slow variables (W(T), B(T)), with a constant precipitation rate P_0 , then we would obtain the same instability boundary. Specifically, we find that there is a transcritical bifurcation, which produces the uniform vegetation solution, when $P_0 = P_c = LM/C\Gamma = \mathcal{MAP}_c$ for

$$\begin{split} \dot{W} &= P_0 - (L + \Gamma B)W, \\ \dot{B} &= C \Big(1 - \frac{B}{K_P} \Big) \Gamma BW - MB. \end{split}$$

This transcritical bifurcation marks the stability boundary for the zero-biomass desert state; it's unstable for $\mathcal{MAP} > \mathcal{MAP}_c$. Numerical simulations using parameters given in Table 2 indicate that patterns may stably co-exist with desert well below $\mathcal{MAP}_c \approx 11\,\mathrm{cm}$. Our numerical investigations of pattern collapse reported in section 5.3 are carried out in such a stable co-existence regime using a stochastic rainfall model with an average \mathcal{MAP} of 8 cm.

Pattern-forming instability of the uniform vegetation solution. In contrast to the desert state, we find that the stability region for the uniform vegetation state, to heterogeneous perturbations, depends on details of the rainfall model. Here we describe our linear stability calculations and summarize some of the key findings related to pattern-forming instabilities of the uniform vegetation state.

Let (w_0, b_0) denote soil water and biomass levels of the τ_p -periodic uniform vegetation state at the start of the rainy season. This state exists, with $b_0 > 0$, for $\mathcal{MAP} > \mathcal{MAP}_c$. We evolve it, together with a small spatially periodic perturbation $(\Delta w_{k,0}, \Delta b_{k,0})e^{ikx}$, over one cycle of the periodic rainfall model. The (linearized) Poincaré return map,

$$\mathcal{P}_{\tau_n,k}(w_0, b_0, \Delta w_{k,0}, \Delta b_{k,0}) = (w_0, b_0, \Delta w_{k,1}, \Delta b_{k,1}),$$

has fixed point $(w_0, b_0, 0, 0)$. This map also determines the linear evolution of the perturbation $(\Delta w_{k,0}, \Delta b_{k,0})$, over the period τ_p , to its updated value $(\Delta w_{k,1}, \Delta b_{k,1})$. We quantify this change by a pair of Floquet multipliers, which are the eigenvalues of the linearized Poincaré return map restricted to the perturbations. We denote this two-dimensional linear map by \mathcal{L}_k , i.e.,

(4.2)
$$\begin{pmatrix} \Delta w_{k,1} \\ \Delta b_{k,1} \end{pmatrix} = \mathcal{L}_k \begin{pmatrix} \Delta w_{k,0} \\ \Delta b_{k,0} \end{pmatrix}.$$

The return map, $\mathcal{P}_{\tau_p,k}$, is a composition of maps associated with the fast and slow subsystems. The fast subsystem distributes the water in the soil after a rain pulse of strength h_0 . The associated map, denoted by $\psi_{h_0,k}$, takes the form

(4.3)
$$\psi_{h_0,k}(w,b,\Delta w_k,\Delta b_k) = (w + \alpha h_0, b, \Delta w_k + \Delta \Omega_{h_0,k}, \Delta b_k).$$

Note that the initial biomass $b + \Delta b_k e^{ikx}$ is frozen for the fast system and hence is unchanged. The soil moisture gains a uniform contribution αh_0 and, for the linearized problem, a nonuniform contribution $\Delta \Omega_{h_0,k} e^{ikx}$. We determine the latter by linearizing (3.13) about $\Delta b_k = 0$, and setting $y_{\ell}(x) = x + \ell_0 + \delta \ell_k(x)$, where

$$\ell_0 = \frac{\nu(b)}{\iota(b)} \ h_0$$

is the distance surface water of height h_0 travels, over uniform biomass at level b, before completely infiltrating into the soil. The change in this travel distance due to the biomass perturbation $\Delta b_k e^{ikx}$, denoted by $\delta \ell_k(x)$, is determined below. First, to linear order in Δb_k and $\delta \ell_k(x)$, we find

$$\Omega(x) = \alpha \iota(b + \Delta b_k e^{ikx}) \int_x^{y_\ell(x)} \frac{\Theta(h_0 - \hat{h}(y; y_\ell(x)))}{\nu(b + \Delta b_k e^{iky})} dy$$

$$= \alpha \left(\iota(b) + \frac{d\iota}{db} \Delta b_k e^{ikx}\right) \int_x^{x + \ell_0 + \delta \ell_k(x)} \left(\frac{1}{\nu(b)} - \frac{1}{\nu(b)^2} \frac{d\nu}{db} \Delta b_k e^{iky}\right) dy + \cdots$$

$$= \alpha h_0 + \alpha h_0 \left[\frac{\delta \ell_k(x)}{\ell_0} + \left(\frac{1}{\iota(b)} \frac{d\iota}{db} + \frac{i(e^{ik\ell_0} - 1)}{\nu(b)k\ell_0} \frac{d\nu}{db}\right) \Delta b_k e^{ikx}\right] + \cdots,$$

$$= \Delta \Omega_{h_0,k} e^{ikx}$$

where the ellipses refer to higher order terms in Δb_k and $\delta \ell_k$. To find the slight adjustment, $\delta \ell_k(x)$, to the total travel distance to complete infiltration at location x, which is specifically due to the biomass perturbation $\Delta b_k e^{ikx}$, we solve $\hat{h}(y_\ell(x); y_\ell(x)) = h_0$ using (3.12). We find, to linear order in Δb_k ,

(4.6)
$$\frac{\delta \ell_k(x)}{\ell_0} = \left[\frac{1}{\nu(b)} \frac{d\nu}{db} e^{ik\ell_0} + \frac{i}{\nu(b)k\ell_0} \frac{d\nu}{db} \left(e^{ik\ell_0} - 1 \right) \right] \Delta b_k e^{ikx}.$$

Combining (4.5)–(4.6), we obtain, for $k \neq 0$,

$$(4.7) \qquad \Delta\Omega_{h_0,k} = \alpha h_0 \left[\frac{1}{\iota(b)} \frac{d\iota}{db} + \frac{1}{\nu(b)} \frac{d\nu}{db} e^{ik\ell_0} + \frac{i}{k\ell_0} \left(\frac{1}{\iota(b)} \frac{d\iota}{db} + \frac{1}{\nu(b)} \frac{d\nu}{db} \right) \left(e^{ik\ell_0} - 1 \right) \right] \Delta b_k.$$

Here, ℓ_0 is given by (4.4), and

$$\frac{1}{\iota(b)}\frac{d\iota}{db} = \frac{(1-f)}{(b+f)(b+1)}, \quad \frac{1}{\nu(b)}\frac{d\nu}{db} = -\left(\frac{\eta}{1+\eta b}\right)$$

follow from (3.5). (Note that for k=0 it can be shown that $\Omega_{h_0,0}=0$.)

The flow map that applies between pulses is derived from the slow system (3.6). It consists of the nonlinear equations satisfied by the uniform vegetation state (w,b), together with the linear equations in the perturbations $(\Delta w_k, \Delta b_k)$. We denote this map, which flows from an initial condition $(w_0, b_0, \Delta w_{k,0}, \Delta b_{k,0})$ for a time τ , by

(4.8)
$$\varphi_{\tau,k}(w_0, b_0, \Delta w_{k,0}, \Delta b_{k,0}) = (w(\tau), b(\tau), \Delta w_k(\tau), \Delta b_k(\tau)).$$

Here, $w(\tau), b(\tau), \Delta w_k(\tau), \Delta b_k(\tau)$ satisfy

(4.9a)
$$\frac{dw}{d\tau} = -(\sigma + \gamma b)w,$$

$$\frac{db}{d\tau} = \left(1 - \frac{b}{\kappa}\right)wb - b,$$

(4.9c)
$$\frac{d\Delta w_k}{d\tau} = -(\delta_w k^2 + \sigma + \gamma b)\Delta w_k - \gamma w \Delta b_k,$$

(4.9d)
$$\frac{d\Delta b_k}{d\tau} = \left(1 - \frac{b}{\kappa}\right) b\Delta w_k + \left(-\delta_b k^2 + w - \frac{2b}{\kappa} w - 1\right) \Delta b_k.$$

We can now construct the Poincaré return map (4.1) as

$$\mathcal{P}_{\tau_p,k} = \varphi_{\tau_d,k} \circ \underbrace{(\varphi_{\Delta\tau,k} \circ \psi_{h_0,k}) \circ \cdots \circ (\varphi_{\Delta\tau,k} \circ \psi_{h_0,k})}_{N_p \text{ times}}.$$

Here, $\Delta \tau = \tau_r/N_p$, which is the time between rain pulses during the rainy season, while $\tau_d = \tau_p - \tau_r$ is the length of the dry season. Restricting the map to the two perturbation components determines \mathcal{L}_k in (4.2). The eigenvalues, λ_k , of \mathcal{L}_k are the (complex) Floquet multipliers. (Note that it follows from (4.7) that the map itself has complex entries.) If the modulus of either eigenvalue λ_k exceeds one, then the uniform state is unstable to pattern-forming perturbations of wavenumber k.

Figure 5 presents, in dimensioned quantities, an example of typical linear stability results for the parameters of Table 2. To obtain these results, we first numerically compute the uniform vegetation fixed point $(w_0, b_0, 0, 0)$ of the Poincaré return map (4.1) and then numerically compute its linear stability via the eigenvalues λ_k of the perturbation map (4.2). Figure 5(a) shows a heat map of the largest $|\lambda_k|$ as a function of both mean annual precipitation \mathcal{MAP} and perturbing wavenumber k in the case of a fixed number of rainstorms per season $N_p = 8$. (For $N_p = 8$, storm strengths range between $H_0 \approx 0.68 \,\mathrm{cm}$ and $H_0 \approx 2.7 \,\mathrm{cm}$ for Figure 5(a).) We find that as \mathcal{MAP} decreases from a high value of $\mathcal{MAP} = 45 \,\mathrm{cm}$, by continuously decreasing H_0 , the uniform state loses stability at $\mathcal{MAP} \approx 42.8 \,\mathrm{cm}$ to perturbations of wavenumber $k \approx 0.141 \,m^{-1}$ (wavelength $L \approx 45 \,\mathrm{m}$). This figure, which shows the instability boundary associated with $|\lambda_k| = 1$ as a black curve, captures a structure in the form of "resonance tongues." Specifically, we find that the instability regions straddle predictions based on overland water flow distances $L_n = 2\ell_0/(n+1)$, $n = 0, 1, 2, \ldots$ (solid white lines), where ℓ_0 is given by (4.4). (For this, we evaluate $\nu(b)$ and $\iota(b)$ in ℓ_0 using the fixed point value b_0 associated with the return map (4.1), i.e., its level at the start of the rainy season.) We find that the most unstable

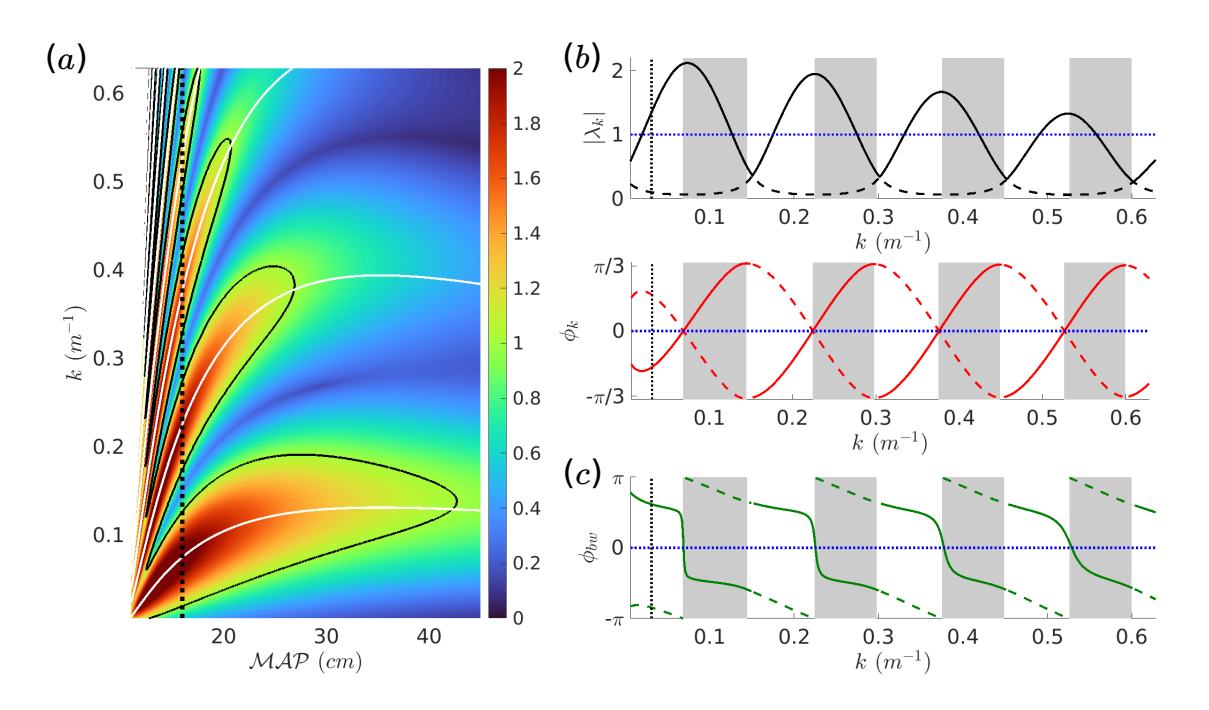


Figure 5. (a) Magnitude of leading eigenvalue of \mathcal{L}_k , defined by (4.2), as a function of mean annual precipitation (MAP) and perturbation wavenumber k. Solid black lines are linear stability boundaries, and solid white lines indicate predicted resonances between the pattern wavelength and characteristic surface flow distance. (b) The magnitude and phase of the two eigenvalues λ_k along the dotted black line at MAP = 16 cm in panel (a). The solid lines correspond to the larger magnitude eigenvalue, and the dashed correspond to the smaller one. Shaded regions yield downhill migration of perturbations, inferred from the sign of ϕ_k . (c) The phase of the biomass perturbation relative to the soil water perturbation associated with the eigenvectors for eigenvalues shown in (b). The wavenumber corresponding to a wavelength of 200 m is marked by black vertical dotted lines in the right panels; compare to nonlinear pattern with same wavenumber in Figure 6.

perturbation has a wavelength L_0 that is well-approximated by twice the distance water flows on the surface before getting infiltrated, i.e., to the perturbation wavenumber $k = \pi/\ell_0$. Thus, at the linear level, the "preferred" pattern wavelength is one for which the newly forming vegetation band harvests water from the location of the newly forming bare soil region. This instability appears as part of a series of increasingly weaker and narrower instability regions, which correspond to the surface water from a newly forming bare soil region traveling n wavelengths before reaching a newly forming vegetation band. Figure 5(b) shows a plot of $|\lambda_k|$ for $\mathcal{MAP} = 16$ cm, indicated by a black dotted line in panel (a), which slices through four of the instability tongues of Figure 5(a).

In order to determine linear predictions for vegetation band migration speed, we extract the phases ϕ_k of the eigenvalues $\lambda_k = |\lambda_k| e^{i\phi_k}$ of \mathcal{L}_k . The second panel of Figure 5(b) shows a plot of ϕ_k , for both eigenvalues λ_k for $\mathcal{MAP} = 16\,\mathrm{cm}$, and indicates that, for all four instability intervals, the phase switches sign near each successive peak of $|\lambda_k|$, and that the phase is confined to an interval around $\phi_k = 0$, here approximately $[-\pi/3, \pi/3]$. If the phase is negative for the unstable Floquet multiplier, then that indicates a phase advance of the pattern during each seasonal cycle and thus corresponds to uphill migration of the vegetation

bands. The opposite holds for a positive phase, shaded gray in panels (b) and (c), which indicates a downhill migration of the vegetation bands. Figure 5(c) shows the phase shift between the components Δw_k and Δb_k of the eigenvectors of \mathcal{L}_k ; e.g., the eigenvector can be written $(\Delta w_k, \Delta b_k) = (1, \mathcal{R}e^{i\phi_{bw}})$, where $\mathcal{R} > 0$ is real. We see that the sign of the phases ϕ_k in Figure 5(b) are (typically) opposite to the phase denoted by ϕ_{bw} in Figure 5(c). This observation lends itself to a simple interpretation. Specifically, if $\phi_{bw} > 0$, then the water peak is uphill from the biomass peak and we might expect uphill migration of the bands, i.e., $\phi_k < 0$. Similarly, we expect $\phi_k > 0$ (downhill migration) if $\phi_{bw} < 0$, in which case the water peak is shifted downhill from the biomass one.

We note that the prediction, of the linearized problem, that patterns might travel downhill is not consistent with observational studies, which report only upslope colonization. Moreover, the observed migration speeds for the bands are slow; for instance, by an order of magnitude, a band might take a century to migrate uphill by one wavelength [11, 23], which would correspond to a (negative) phase shift of $\sim \pi/100$ every seasonal cycle. In the subsequent sections, we explore how well these linear findings hold up for the nonlinear problem under periodic and stochastic rain inputs.

4.2. Nonlinear patterns. Numerical simulations indicate that, while the linear theory captures the behavior of small amplitude patterns near the onset of the lowest order resonance tongue shown in Figure 5, the nonlinear patterns selected at lower \mathcal{MAP} values exhibit dynamics very different from the linear predictions. Even still, the importance of the characteristic distance surface water travels before infiltrating into the soil seems to carry over into the nonlinear regime, as we now demonstrate.

For Figure 6, we consider periodic rainfall with $\mathcal{MAP} = 16 \,\mathrm{cm}$ and storm depth of $H_0 =$ 1 cm on a 1 km domain. Simulations initialized with the 0.1% random noise on top of the uniform vegetation state typically settle into a "traveling-wave" state with five bands on the domain. Here we use "traveling wave" (in quotes) to indicate that the state undergoes a spatial translation under the nonlinear map associated with evolving the system by one rainy and subsequent dry season. The five-band state (wavelength of 200 m, wavenumber of $\sim 0.0314 \, m^{-1}$) has an uphill migration speed of approximately $69 \, \mathrm{cm/year}$, corresponding to translation by one wavelength every ~ 290 years; this wavenumber is also indicated by a vertical line in the linear results of Figure 5(b). Panel (a) provides timeseries data of spatially averaged quantities over the last 2 years of the 100-year simulation, panel (b) shows spatial profiles derived from the last year of the simulation, and panel (c) shows annually averaged spacetime plots. We note that $\Delta Y_{\ell}(X)$ in panel (b) is the farthest (dimensioned) distance traveled by water on the surface during a rainstorm before infiltrating at a point X. The dimensionless version of this quantity is $\Delta y_{\ell}(x) \equiv y_{\ell}(x) - x$, where y_{ℓ} is defined in section 3.2 and sets the upper bound of integration for computing the soil water kick Ω in (3.13). The linear stability analysis of spatially uniform states in section 4.1 indicates that $\Delta y_{\ell}(x) = \ell_0$, a constant value in this case, plays a key role in controlling the wavelength of the patterns. For the fully nonlinear patterns shown in Figure 6, we see a "sawtooth" structure in the plot of the average $\Delta Y_{\ell}(x)$. Gray horizontal arrows indicate the farthest average distance traveled by water that infiltrates into locations between the peak value of $\Delta Y_{\ell}(X) = 180 \,\mathrm{m}$ at $X = 321 \,\mathrm{m}$ and the minimum value of $\Delta Y_{\ell}(X) = 36 \,\mathrm{m}$ at $X = 478 \,\mathrm{m}$. Water initialized at $X = 514 \,\mathrm{m}$, within the trailing edge of a vegetation band, travels through nearly the entire vegetation

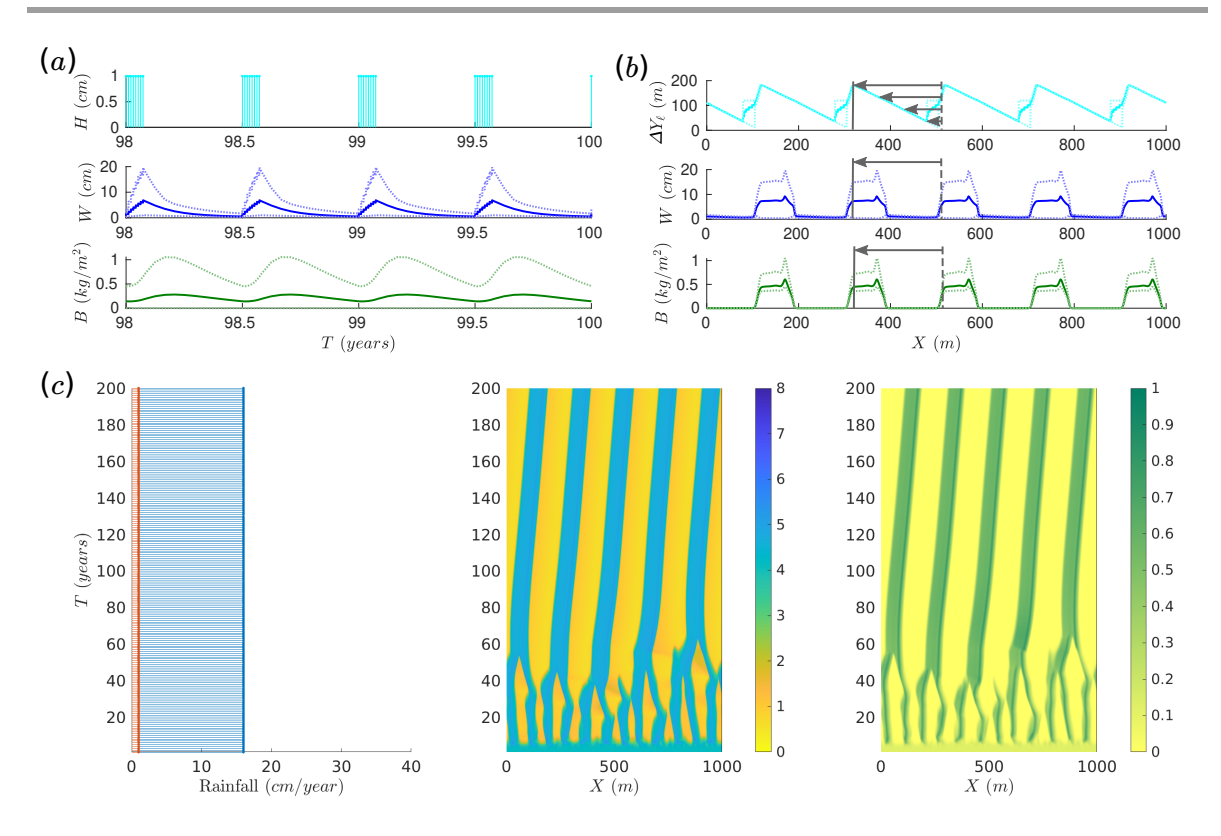


Figure 6. (a) Time series showing, from top to bottom, storm depth H of rain pulses, domain-averaged soil water W, and biomass B during last two years of a 100-year simulation under periodic rainfall. Solid lines indicate spatially averaged fields, while dashed lines indicate instantaneous min/max. (b) Spatial distribution, from top to bottom, of dimensioned maximum distance $\Delta Y_{\ell}(X)$ traveled by water before infiltrating, soil water W, and biomass B during the last year of the simulation. Solid lines indicate averages over rainstorms for $\Delta Y_{\ell}(X)$ and annual averages for W and B. Pointwise min/max values are shown by dashed lines. Horizontal gray arrows have length equal to $\Delta Y_{\ell}(X)$ and indicate the farthest distance traveled by surface water infiltrating into locations at the arrow tips. (c) From left to right, time series of annual rainfall totals in blue with 1 cm contribution from each rainstorm highlighted in orange, spacetime plots of annually averaged soil water in units of cm, and biomass in units of kg/m². Parameters: Periodic rainfall with $\mathcal{MAP} = 16$ cm, storm depth $H_0 = 1$ cm, and rainy season duration $T_r = 1$ month on an L = 1000 m domain and initialized with 1% random noise on top of the spatially uniform solution.

band downhill before fully infiltrating. This indicates that nearly the entire 86 m width of the vegetation bands are harvesting water from bare soil regions uphill of them and that none of the water travels across a band into the bare soil region downhill of it.

Using the same parameters, we also observe a state with six bands that migrate downhill at an average rate of about $179\,\mathrm{cm/year}$ or one $L\approx 167\,\mathrm{m}$ wavelength every 93 years. Figure 7 zooms in on a single band of these 5-band and 6-band periodic patterns. It shows, from bottom to top, the spatial profiles of the biomass B and the maximum distance ΔY_ℓ water travels before infiltrating into the soil for each of the eight one-centimeter rainstorms of a rainy season. The profiles are aligned so that X=0 corresponds to the farthest downhill that water initialized within the vegetation band reaches during any of the rainstorms. With this choice, if there is a bare soil region uphill of the vegetation band, then we know that it did not collect water from a vegetated region during the rainy season.

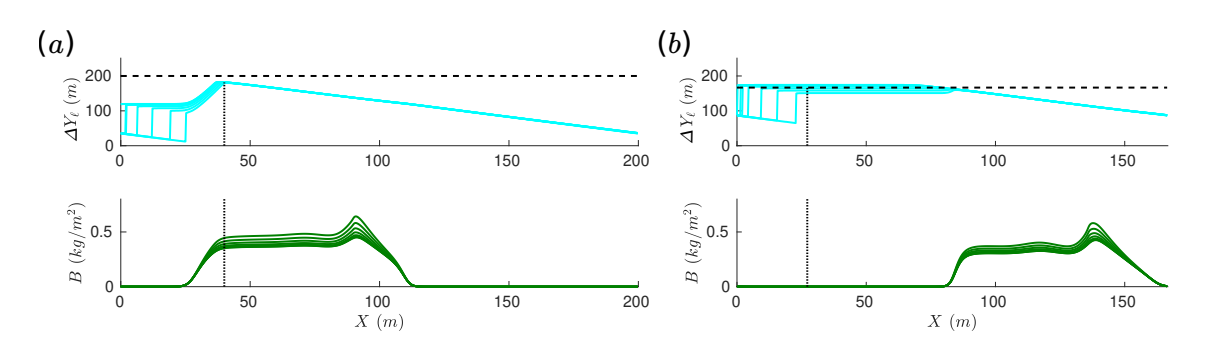


Figure 7. Spatial distribution of maximum distance $\Delta Y_{\ell}(X)$ traveled by water before infiltrating and biomass profile associated with each of the eight rainstorms during one season with (a) $L=200\,\mathrm{m}$ with average uphill migration speed of 69 cm/year and (b) $L\approx 167\,\mathrm{m}$ with average downhill migration 179 cm/year. The location of the peak of $\Delta Y_{\ell}(X)$ averaged over the eight storms is marked by a vertical dotted line, while the domain size is marked by a horizontal dashed line. Parameters: Periodic rainfall with $\mathcal{MAP}=16\,\mathrm{cm}$, storm depth $H_0=1\,\mathrm{cm}$, and rainy season duration $T_r=1\,\mathrm{month}$.

The uphill-migrating case with $L=200\,\mathrm{m}$ in panel (a) is more "optimal" in the sense that the water from the bare region uphill of the band is deposited completely within the band, as evidenced by the peak value of ΔY_{ℓ} being less than the domain length. Moreover, the peak is located within the vegetation band. By contrast, the profile of ΔY_{ℓ} in the downhill migrating case with $L\approx 167\,\mathrm{m}$, shown in panel (b), indicates that water is traveling all the way across the band and continuing into the downhill bare soil region. The peak values for ΔY_{ℓ} in this case, which is about 174 m, slightly exceeds the domain length.

5. Stochastic rainfall. In this section, we explore some of the striking differences in behavior of the pulsed-precipitation model under stochastic rainfall, compared to the idealized periodic rainfall results of section 4. Numerical simulations indicate that banded patterns still form under stochastic rainfall, with characteristics consistent with observational data for band spacing and migration speed. Moreover, some of the more complex, and perhaps worrisome, spatiotemporal behaviors produced by the model with idealized periodic rainfall vanish once stochasticity in rainfall is introduced. We also find that the variability in rainfall can lead to noise-induced transitions from a patterned state to the bare soil state when the mean annual precipitation level puts the system in a bistable regime, below the transcritical bifurcation point found in section 4.1. We show that both the rainfall and the vegetation band characteristics can impact statistics of these collapse events.

We assume $N_s = 2$ equal rainy seasons per year, each lasting T_r days. The intervening dry seasons last for a time $T_d = T_y/N_s - T_r$, where $T_y = 365$ days. During each rainy season we model the rainstorms as a Poisson point process with a mean arrival rate of $\lambda_r = \mathcal{MAP}/H_0/N_s/T_r$ where \mathcal{MAP} is the mean annual precipitation and H_0 is the mean rainfall per storm. The actual amount of rainfall H_i , in the *i*th storm, is drawn from an exponential distribution with mean H_0 , where we typically consider $0.5 \le H_0 \le 2$, measured in cm. While $T_r = 1$ month is our default value, we let $T_r \to 0$ to speed up computations for the ecosystem collapse simulations of section 5.3, after first exploring some of the effects of changing the rainy season duration in section 5.2.

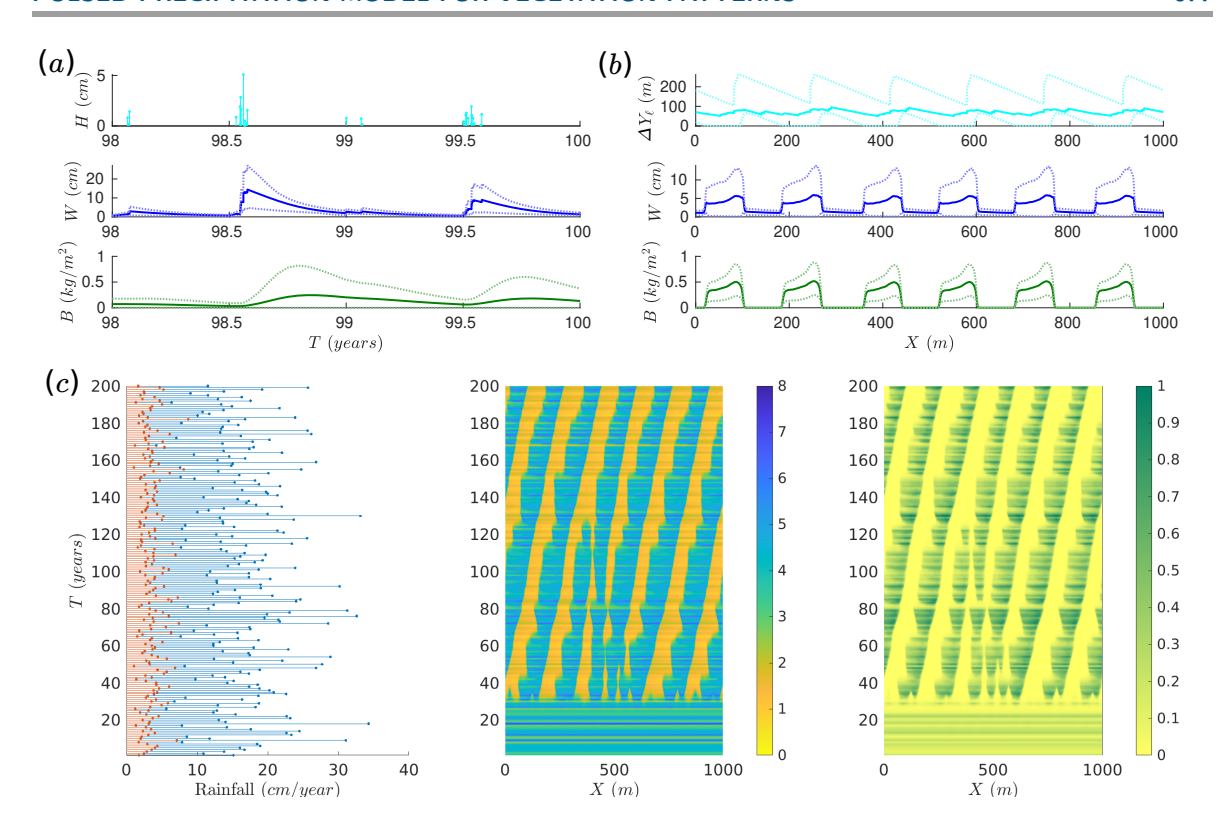


Figure 8. (a) Time series showing, from top to bottom, storm depth H of rain pulses, domain-averaged soil water W, and biomass B during the last two years of a 100-year simulation under periodic rainfall. Solid lines indicate spatially averaged fields, while dashed lines indicate instantaneous min/max. (b) Spatial distribution, from top to bottom, of dimensioned maximum distance $\Delta Y_{\ell}(X)$ traveled by water before infiltrating, soil water W, and biomass B during the last year. Solid lines indicate averages over rainstorms for $\Delta Y_{\ell}(x)$ and annual averages for W and B. Pointwise min/max values are shown by dashed lines. (c) From left to right, time series of annual rainfall totals in blue with contribution from largest rainstorm highlighted in orange, spacetime plots of annually averaged soil water, and biomass. Parameters: Stochastic rainfall with $\mathcal{MAP} = 16 \, \mathrm{cm}$, mean storm depth of $H_0 = 1 \, \mathrm{cm}$, and $T_r = 1 \, \mathrm{month}$ on an $L = 1000 \, \mathrm{m}$ domain and initialized with 1% random noise on top of the spatially uniform solution.

Figure 8 shows an example of results from a simulation on a 1 km domain initialized with 0.1% random noise on top of the uniform vegetation state, $\mathcal{MAP} = 16 \,\mathrm{cm}$, and mean storm depth $H_0 = 1 \,\mathrm{cm}$. The simulation settles into a "stochastic traveling wave" solution which fluctuates from season to season, due to rainfall variability, but can be characterized by a mean vegetation band width, spacing, and migration speed. In this case the pattern consists of 6 bands on the domain and travels uphill on average, which is in contrast to the 6-band pattern obtained with periodic rainfall in section 4.2, which traveled downhill. We also note that the annual mean ΔY_{ℓ} in the last year, shown in Figure 8(b), has an average of 94 m, which is approximately half the wavelength of the pattern, which is $\sim 167 \,\mathrm{m}$. This ratio, at ~ 0.56 , is remarkably in line with the resonance tongue phenomenon explored in section 4.1.

5.1. Comparison to periodic rainfall. In repeated trials of the stochastic simulation, with parameters as in Figure 8, we typically observe between 5 and 12 bands on the 1000 m

domain at 200 years. This is in contrast to the skewed-lower and narrower range of 4 to 6 bands observed under periodic rainfall as described in section 4.2. We also see occasional, intermittent collapse of the vegetation to the bare soil state and explore this phenomenon further in section 5.3 at lower precipitation levels where the vegetation cannot recover.

Comparing Figures 6 and 8 shows that while fluctuations in the size and number of rainstorms per season drive fluctuations in the soil water-biomass dynamics, there are qualitative similarities between the mean pattern characteristics in the stochastic rainfall case and the periodic rainfall one. However, Figure 9, which further compares the pattern characteristics of periodic and stochastic rainfall, shows that this is not always the case. To generate those results, we fixed the rain model parameters to have $\mathcal{MAP} = 16\,\mathrm{cm}$ and (mean) storm depth $H_0 = 1 \,\mathrm{cm}$, and we enforced different band spacings by changing the size of the periodic domain L and initializing with a perturbation of wavenumber $k = 2\pi/L$. We restricted ourselves to $L \le 250 \,\mathrm{m}$ since for domains with $L > 250 \,\mathrm{m}$ ($k < 0.0252 \,\mathrm{m}^{-1}$) the initial perturbation would split and the pattern eventually settled into a multiband state on the domain. At $L=250\,\mathrm{m}$, we obtained a single-band "traveling wave" state for the periodic rainfall case, while the stochastic rainfall case still split into two bands. For cases with $100 < L < 167 \,\mathrm{m}$ and $L < 59 \,\mathrm{m}$, we did not observe "traveling wave" states with periodic rainfall but did observe a "stochastic traveling wave" state with stochastic rainfall. The intervals in L for which one or both rainfall models did not reach a "(stochastic) traveling wave state" are shaded gray in Figure 9(a-c). We observed relatively consistent values of average biomass on the domain but with a gradual increase in fraction of the domain covered as a function of k. Figure 9(c) shows migration frequency for these simulations. We compute the migration speed by tracking the motion of the uphill edge of the vegetation band whenever there is a clearly defined band. We take the edge as the location where the biomass first goes above a threshold value of $\epsilon_B = Q/5 = 0.02 \,\mathrm{kg/m^2}$. While we see significant downhill migration with periodic rainfall, the stochastic simulation bands tend to travel slowly uphill (on average), except in a few cases with very short domain sizes.

5.2. Dependence on rainy season duration. In this subsection we investigate the impact of changing the duration of the rainy season on pattern characteristics, as well as on mean time to ecosystem collapse at low mean annual rainfall. This investigation is motivated in part by an additional computational speedup that is possible if we take $T_r \to 0$ so that all rainstorms in a given rainy season occur simultaneously. In this limit we can use the same biomass profile for all the storms, thereby admitting an efficient parallel computation of the associated soil water contributions Ω by (3.13). Exploring the impacts of rainy season duration is also of possible interest in light of observed changes in the rainfall seasonality of Eastern Africa [50].

Simulations at $\mathcal{MAP} = 16 \,\mathrm{cm}$ indicate very little dependence of pattern characteristics on the duration of a rainy season for $0 < T_r \lesssim 3 \,\mathrm{months}$, aside from an approximate 10 - 30% increase in migration speed for each month of added rainy season duration. At a lower \mathcal{MAP} value of 8 cm, where the bare soil state stably co-exists with patterns, simulations initialized with a banded vegetation state may transition to the stable bare soil state and not recover on a centuries-long simulation timescale. In practice, we identify these collapse events by tracking the domain-averaged biomass; we use a threshold of $\epsilon_B = Q/5 = 0.02 \,\mathrm{kg/m^2}$ and require the biomass level to stay below that for at least one decade. Figure 10(a)–(c) illustrates a collapse

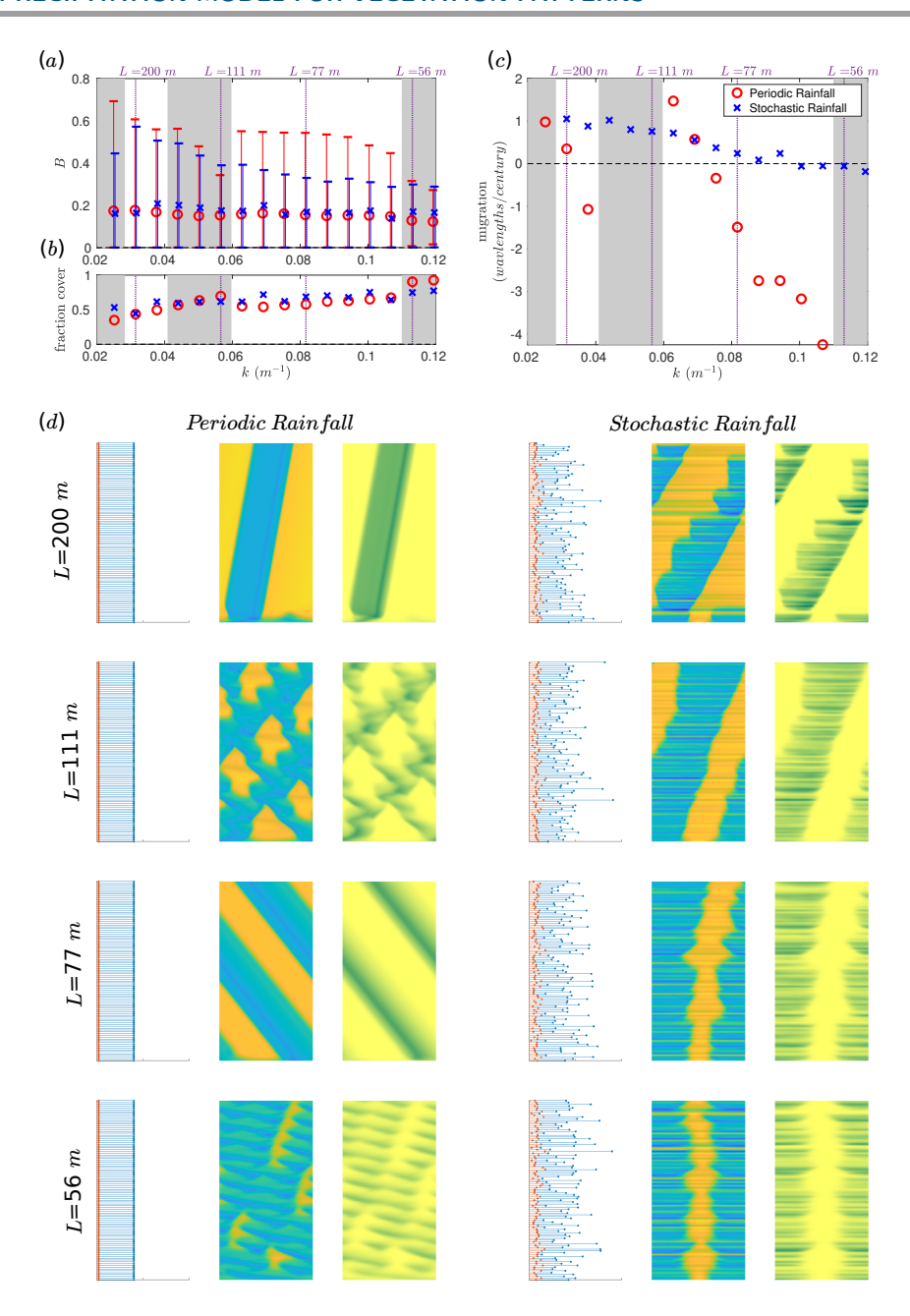


Figure 9. Comparison of pattern characteristics under periodic and stochastic rainfall. (a) Minimum, maximum, and mean of annually averaged biomass profile, (b) fraction of domain covered by biomass, and (c) mean migration speed as a function of pattern wavenumber $k=2\pi/L$ for one band on a periodic domain of length L. Results from simulations under periodic rainfall are marked with red circles and stochastic rainfall with blue x's. Either "traveling waves" or "stochastic traveling waves" were not obtained from simulations with domain sizes appearing within the gray shaded regions. Thumbnails of annual rainfall, soil water, and biomass from example simulations are shown in panel (d) at the domain sizes indicated in the panels above for both (left) periodic rainfall and (right) stochastic rainfall. The vertical time axis covers 100 years, and the horizontal rainfall axis goes to 40 cm in all of the cases, while each row has a different scale on the horizontal spatial axis for soil water and biomass in order to show the entire periodic domain. Color scales are the same as in Figures 6 and 8.

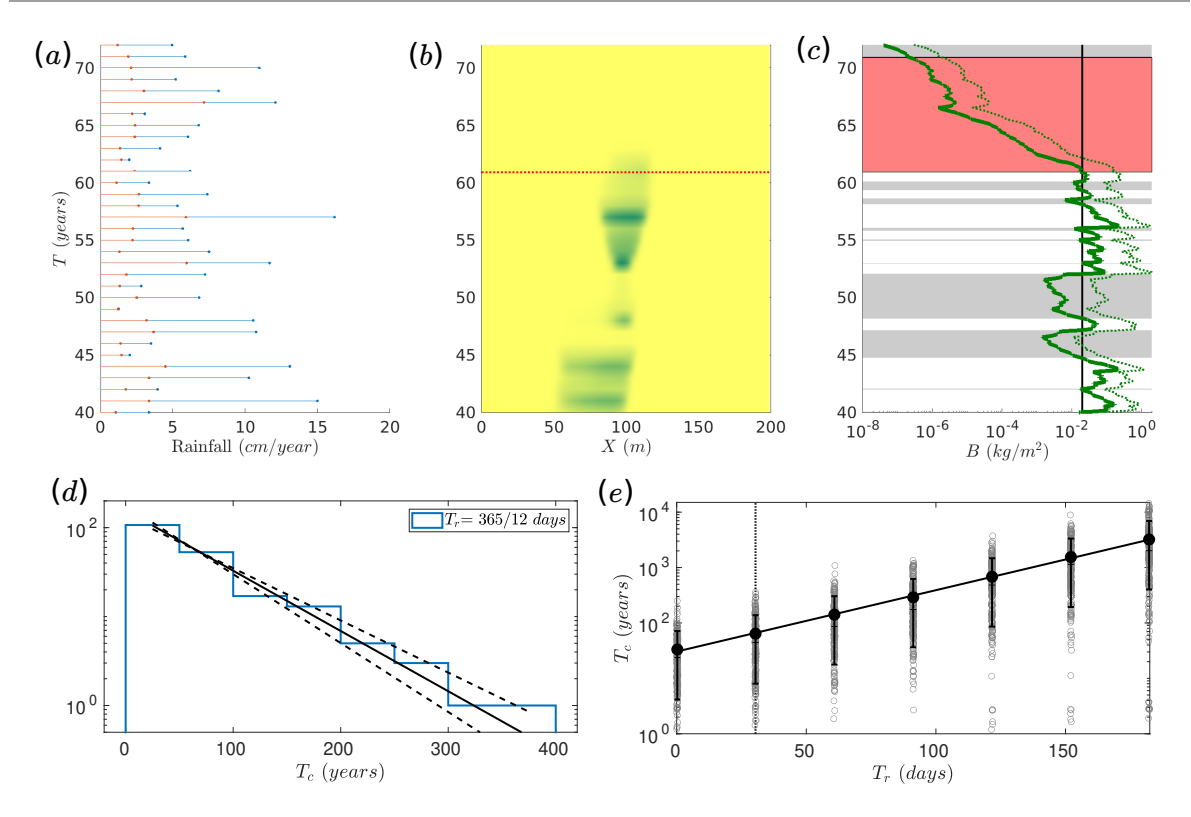


Figure 10. (a) Annual rainfall and (b) biomass distribution starting at T=40 years for a stochastic rainfall simulation with $\mathcal{MAP}=8\,\mathrm{cm}$, $H_0=1\,\mathrm{cm}$, and $T_r=1\,\mathrm{month}$ on an $L=200\,\mathrm{m}$ domain that collapses at $T\approx61$ years. (c) Collapse is defined when the mean biomass on the domain, indicated by the solid green line, falls below $\epsilon_B=0.02\,\mathrm{kg/m^2}$ for 10 consecutive years (shaded red). All (shorter) intervals with $B_{avg}<\epsilon_B$ are shaded gray. The dashed green line indicates the peak biomass value on the domain as a function of time. (d) A histogram of collapse times from 200 trials with the parameters from (a)–(c), and indicated by a dotted vertical line in (e), has a mean survival time of $T_c=64$ years. The solid black line represents an exponential distribution with this mean, and the dashed lines represent a 95% confidence interval for a maximum-likelihood fit of the histogram to an exponential distribution. (e) The mean survival time approximately follows an exponential trend as a function of the duration of the rainy season T_r . Each gray circle represents a single simulation, while the solid black circles indicate the mean over 200 trials at each value of T_r , and the vertical bars indicate 95 confidence interval for the fit of the trails T_r to an exponential distribution. The data fits well the solid black line, $T_c=30.5\times2.2^{T_r}$, with T_r given in months and T_c given in years.

event for a sample simulation at $\mathcal{MAP} = 8 \,\mathrm{cm}$, $H_0 = 1 \,\mathrm{cm}$, and a 1-month rainy season on an $L = 200 \,\mathrm{m}$ domain. Time intervals for which the average biomass, shown in Figure 10(c), falls below the threshold are shaded in gray, while the first interval that lasts 10 years is shaded red. Survival times for 200 trials with the same parameters, shown in Figure 10(d), are well-approximated by an exponential distribution. We use the same 200 rain sequences and rescale the relative wait times by a constant factor to obtain a range of rainy season durations between simultaneous rainstorms $(T_r \to 0)$ and year-round rainfall $(T_r = 6 \,\mathrm{months})$. A plot of the survival times as a function of duration of the rainy season, shown in Figure 10(e), indicates that the mean survival time from the exponential fit approximately doubles with each additional month of increase in rainy season duration.

5.3. Collapse at low precipitation values. We now explore the dependence of collapse on rainstorm intensity and band spacing. We assume that all the rainstorms in each season occur simultaneously so that we may take advantage of the computational speed up noted in section 5.2 for $T_r \to 0$. Since this may bias the collapse events towards shorter times, as suggested by results in Figure 10(e), we keep the focus on the trends associated with varying certain parameters.

We conduct trials with stochastic rainfall at $\mathcal{MAP} = 8\,\mathrm{cm}$, where stable "traveling wave" patterns exist under periodic rainfall. With stochastic rainfall, there is inevitably a collapse to the (bistable) bare soil in simulations initialized with a single vegetation band on a domain of $50 \leq L \leq 1000\,\mathrm{m}$ and mean rainstorm depth $0.4 \leq H_0 \leq 2\,\mathrm{cm}$. Here, as illustrated in Figure 10(a-c), we define collapse to be when the domain-averaged biomass level first falls below $\epsilon_B = Q/5 = 0.02\,\mathrm{kg/m^2}$ and remains so for a period of 10 years, at which point we terminate the simulation. We generate the initial condition for the stochastic simulations via a periodic rainfall simulation with an identical sequence of rainstorm depths in each season, run to its steady state. For this, rather than choosing each storm in the sequence to have the same strength, we take the expected number of storms (rounded to nearest integer) that we will use for the stochastic model and select the storm depths to match expected values for storm intervals of equal probability for the exponential distribution. We find that selecting the initial condition in this way avoids premature collapse due to the initial condition not being appropriately "tuned" to the rainfall pattern.

We begin with an exploration of rainfall statistics near collapse. Figure 11(a) shows time series of the domain-averaged biomass and seasonal rainfall in the 20-year window surrounding collapse in a stochastic rainfall simulation with $\mathcal{MAP} = 8 \,\mathrm{cm}$ and $H_0 = 1 \,\mathrm{cm}$ initialized with a single vegetation band on a 200 m domain. The bottom panel of Figure 11(a) shows a histogram of rainfall events within the shaded 2-year window centered at time $\Delta T_c = -5$ years, which is measured relative to the collapse time $\Delta T_c = 0$. We use this sliding 2-year window for computing rain statistics for the 200 trials. Figure 11(b) then summarizes, from top to bottom, the mean biomass \overline{B} , the mean annual precipitation \mathcal{MAP} , and the mean rainstorm depth \overline{H}_0 for $\Delta T_c \in [-10, 10]$ years. The average over all trials is given in solid black, interquartile ranges are shaded cyan, and the minimum/maximum values are indicated by dotted lines. The red dashed lines indicate the biomass threshold $\epsilon_B = 0.02 \,\mathrm{kg/m}^2$ for collapse, and the expected values of \mathcal{MAP} and \overline{H}_0 are based on the parameters of the rainfall model. There is a noticeable drop in all three quantities in the vicinity of collapse, with biomass, by definition of collapse, failing to recover. These results suggest that the drop in \mathcal{MAP} may be critical to driving collapse; its minimum mean value falls from the expected 8cm to 3.2cm; it does so approximately 5 months after our defined "collapse time." The mean storm depth \overline{H}_0 also drops from its expected 1 cm value to 0.66 cm. However, this does not account for the full deficit in \mathcal{MAP} since we'd expect about 5.3 cm if the mean storm frequency remained at 8 storms per year. The average \mathcal{MAP} , over the trials, falls to a lower value because there is a similar drop (not shown) in the mean number of storms per year, from 8 to approximately 5.

Figure 12(a) shows the survival times, i.e., the length of time before collapse, of stochastic simulations with $\mathcal{MAP} = 8 \,\mathrm{cm}$ and mean rainstorm depth $H_0 = 1 \,\mathrm{cm}$ as a function of domain length L. The mean survival times from exponential fits of 200 trials at each value of L are marked by solid red circles. An increase in the (periodic) domain size, corresponding to an

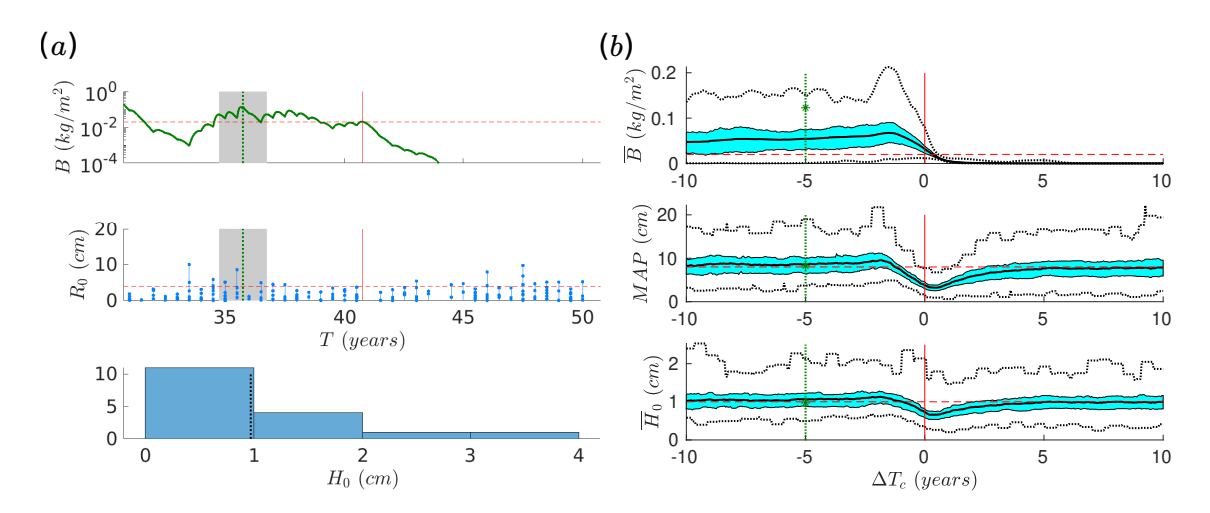


Figure 11. Rainfall statistics near collapse. (a) A time series of domain-averaged biomass is shown for a 20- year interval centered around a collapse event, marked by a vertical red line in the top panel. The middle panel shows the seasonal rainfall, with the contribution from each individual storm marked by dots. The bottom panel shows a histogram of rainstorm depths within the 2-year window highlighted in gray and centered at $\Delta T_c = -5$ years relative to the time of collapse. (b) From top to bottom, average biomass on the domain, mean annual precipitation, and mean storm depth within a 2-year window centered about the time relative to collapse, ΔT_c . The solid black line indicates averages over 200 trials, the shaded cyan region indicates the interquartile range, and the dotted lines indicate the minimum and maximum values. The red dashed line indicates the collapse threshold level for biomass and the expected mean values for the rainfall parameters.

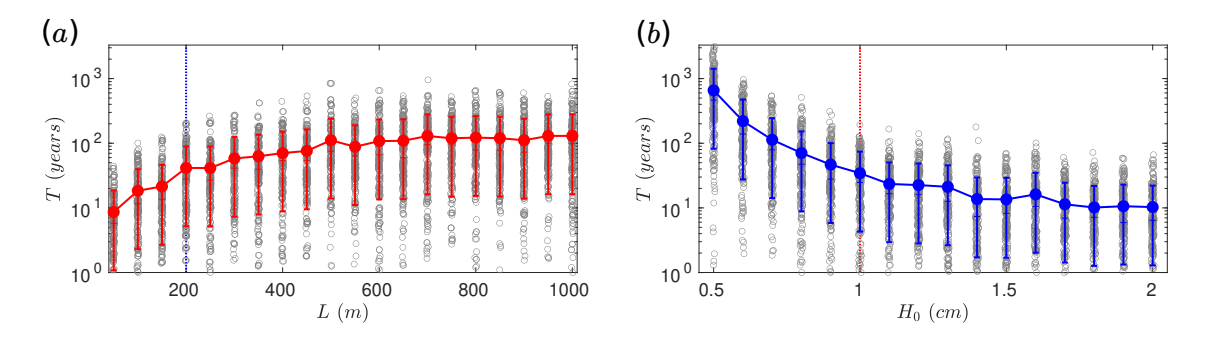
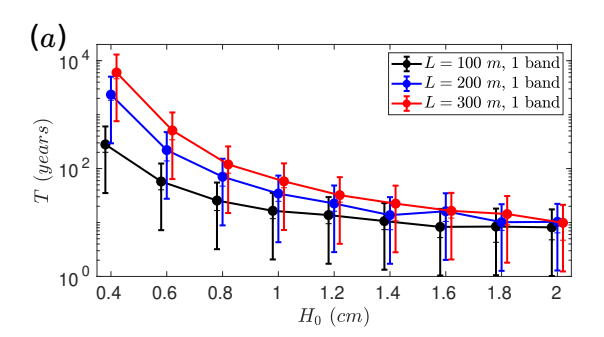


Figure 12. Survival times for simulations under stochastic rainfall with $\mathcal{MAP} = 8\,\mathrm{cm}$ and a single band initialized on the domain as a function of (a) domain length L with mean storm depth $H_0 = 1\,\mathrm{cm}$ and (b) mean storm depth H_0 with domain length $L = 200\,\mathrm{m}$. Each gray circle represents a single simulation, while the red/blue circles indicate the mean of a maximum-likelihood fit of the 200 trials at each parameter value to an exponential distribution and the vertical bars indicate a 95% confidence interval for each fit. A linear interpolation of the mean values highlights the trend that survival times (a) increase as a function of domain size and (b) decrease as a function of mean storm depth.

increase in the spacing between bands in a periodic pattern, leads to longer mean survival time over this range. However, the trend (on the logarithmic scale) appears to saturate for longer domain sizes. Results analogous to those of Figure 12(a), described above, are shown with blue in Figure 12(b) as a function of the mean storm depth H_0 for a fixed domain size of $L = 200 \,\mathrm{m}$. We see longer survival times on average with smaller H_0 , with the trend leveling



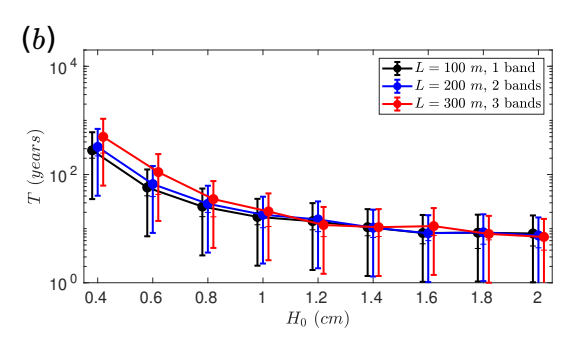


Figure 13. How band spacing affects the dependence of survival times on mean storm depth H_0 for stochastic simulations with $\mathcal{MAP} = 8\,\mathrm{cm}$. (a) A single band is initialized on an $L = 100,\,200,\,$ and $300\,\mathrm{m}$ domain. (b) One, two, and three bands are initialized with $100\,\mathrm{m}$ spacing. The red, blue, and black circles indicate the mean of a maximum-likelihood fit of the 200 trials to an exponential distribution at each parameter value, and the vertical bars indicate a 95% confidence interval associated with each fit. A linear interpolation of the mean values highlights the trends for these simulations. The mean survival times for simulations (a) initialized with a single vegetation band increase with domain size for mean storm depths below approximately $1\,\mathrm{cm}$, yet (b) do not depend strongly on domain size when the band spacing of the initial condition is fixed.

off somewhere above $H_0 \approx 1 \,\mathrm{cm}$. Since \mathcal{MAP} is fixed, smaller storm depths correlate with more storms in each season and also less variability in annual precipitation from year to year.

We find that the mean survival time depends more strongly on H_0 for larger domain sizes when initialized with a single band on the domain. Figure 13(a) shows the average survival times from a maximum-likelihood fit of 200 trials to an exponential distribution at each H_0 for $L=100,\ 200,\$ and 300 m domains. We also observe that increasing the domain size but fixing the band spacing has little effect on trends in mean survival time. Figure 13(b) shows results analogous to those of Figure 13(a) described above, except that the initial condition is chosen for each domain size to fix the band spacing at 100 m. Some of the longer-lived trials initialized with multiple vegetation bands do occasionally prolong survival by first losing one or two bands. However, these partial collapse events are infrequent and have little impact on the overall statistics; the majority of simulations collapse by losing all vegetation bands at once.

6. Discussion. We have developed a pulsed-precipitation model for banded vegetation patterns in dryland ecosystems and used it to investigate the impacts of changing rainfall patterns. The model is built upon the fast-slow modeling framework [18] and leverages additional simplifying assumptions about overland surface water flow and infiltration into the soil to obtain a closed form expression for the soil water contribution from a rainstorm. Biomass and soil water evolve on the slow timescale associated with plant growth, with rainstorms modeled as instantaneous kicks to the soil water, which are spatially dependent as they follow the biomass profile. These soil water kicks capture the positive biomass-water resource feedbacks via enhanced infiltration and reduced surface flow speeds in vegetated zones.

Our pulsed-precipitation model paves the way for exploration of stochastic rainfall patterns by allowing significant computational speedup over the original fast-slow model, thus making large numbers of trials feasible. We note that computational speed has also been addressed by applying machine learning techniques to predict the soil water distribution following rain in a more detailed hydrological model [8]. Although stochasticity and seasonality of rainfall were not considered in that paper, they did include storm duration, along with storm depth, as training parameters, and observed similar qualitative trends of increased band spacing with increased storm depth. An advantage of our approach is that simplifying the model keeps analysis, and the insights gained from it, within reach. Nonetheless, it will be important to characterize the impacts of our simplifications on predictions in future work through comparison to more detailed models.

Linear stability analysis of the model under periodic rainfall reveals that the distance ℓ_0 that water flows on the surface before infiltrating into the soil plays a key role in determining pattern characteristics such as band spacing, a result that has also been suggested in the context of so-called flat-terrain vegetation patterns [47]. With periodic rainfall, the pattern formation in the pulsed-precipitation model is organized around a series of "spatial resonances" in which water from the newly forming bare soil region travels some integer number of wavelengths of the pattern before infiltrating into the newly forming vegetation band. Simulations indicate that while the nonlinear patterns that form are significantly different from those predicted by the linear stability analysis, insights about the key role of the distance surface water flows still apply, even under stochastic rainfall. Nonetheless, some of the predictions obtained under periodic rainfall, such as significant downhill migration of vegetation bands, run contrary to observation. This aspect of the underlying resonance structure, present with the idealized periodic rainfall, is, however, washed out when we introduce variability to the rainfall model; stochastic rainfall simulations produce banded patterns with characteristics that are reasonably consistent with observation. The impact of stochasticity on the existence and stability of nonlinear traveling wave patterns is itself an intriguing mathematical question. For example, how does the so-called Busse balloon, which was investigated in the context of vegetation patterns for a modified Klausmeier model [2, 48], change when rainfall is less predictable? Our investigation of a stochastic and impulsively forced pattern forming system suggests new directions for fundamental pattern formation research.

Motivated by the potential for identifying precursors to ecosystem collapse in a changing climate, a main focus of this study is the transition from spatially patterned vegetation to the desert state. Indeed, at low enough mean annual precipitation values, stable vegetation patterns exist alongside a stable bare soil state, and fluctuations in rainfall can trigger ecosystem collapse. We see that both the pattern characteristics, such as band spacing, and the rainfall characteristics, such as rainy season duration and mean storm depth, have an impact on the mean time to collapse. Increased band spacing, corresponding to a larger area for harvesting water, leads to longer survival times. Both longer rainy seasons, corresponding to shorter dry intervals in which the biomass must survive without rainfall, and less intense storms, corresponding to a decrease in variability of rainfall from season to season, also increase the mean survival time. We note that we have also observed collapse of patterns at higher precipitation levels, but, if the bare soil state is unstable, the ecosystem is expected to recover.

Studies that use mathematical models to investigate the possible impact of a changing climate on vegetation patterns typically do so by varying the mean annual precipitation [1, 44, 46], with all other parameters held fixed. The pulsed-precipitation model allows for exploration of other rainfall characteristics, such as mean storm intensity, seasonality, and other forms of variability. We illustrate the potential here by presenting results from 200 trials with stochastic

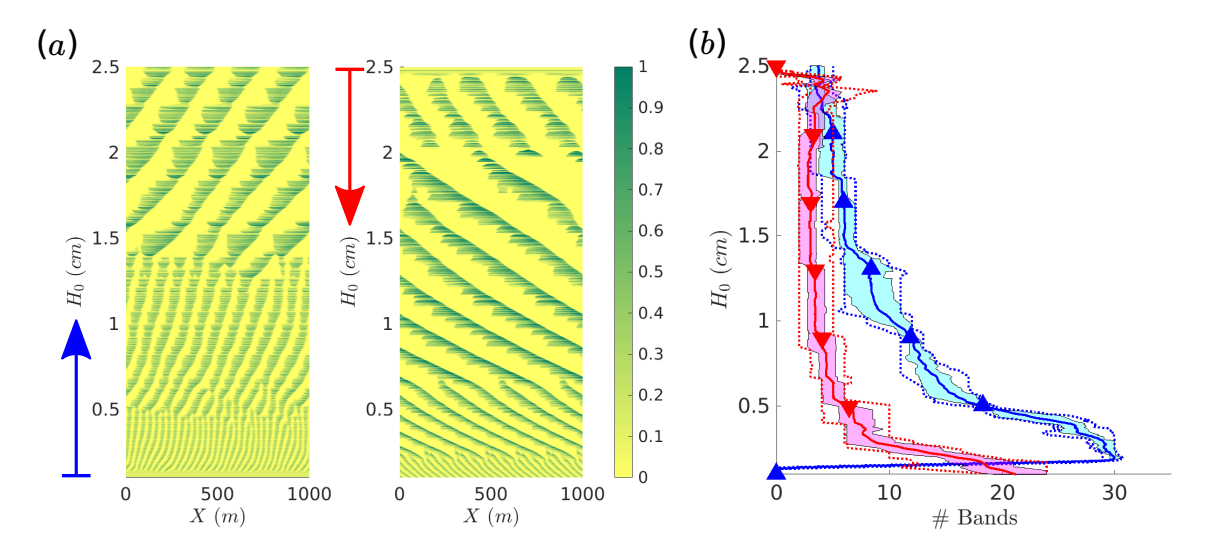


Figure 14. Transitions in band spacing as a function of slowly varying mean storm depth H_0 . (a) Spacetime plots of annually averaged biomass distribution from 1200-year simulations with stochastic rainfall with $\mathcal{MAP} = 16\,\mathrm{cm}$ and rainy season length $T_r \to 0$. The mean storm depth is linearly increased from $H_0 = 0.1\,\mathrm{cm}$ to 2.5 cm at a rate of 2 cm/millennium in the left panel and decreased at the same rate starting from $H_0 = 2.5\,\mathrm{cm}$ in the right panel. The blue and red arrows indicate the direction of time for increasing and decreasing storm depth. (b) The average number of bands from 200 trials of increasing and decreasing H_0 are depicting with the thick blue and red lines marked by up and down triangles. The shaded cyan and magenta regions indicate the interquartile range from the 200 trails at each value of H_0 for increasing and decreasing H_0 . The dotted lines indicate the maximum and minimum number of bands from the trials for each corresponding color.

rainfall at $\mathcal{MAP} = 16 \,\mathrm{cm}$ and $T_r \to 0$ in which the mean storm depth starts at $H_0 = 0.2 \,\mathrm{cm}$ and is then slowly increased to $H_0 = 2.5 \,\mathrm{cm}$ (at a rate of $2 \,\mathrm{mm/century}$). We also carry out another 200 trials with the mean storm depth slowly decreasing from $H_0 = 2.5 \,\mathrm{cm}$ at the same slow rate. (Each of these 400 trials is initialized with uniform vegetation with 1% random noise.) Figure 14(a) shows example spacetime distributions of the annually averaged biomass, where the blue and red arrows indicate the direction of time for the simulations with increasing and decreasing storm intensities. As expected, based on the role of storm depth in pattern selection for the model, the simulations exhibit increased band spacing, on average, at higher H_0 . Figure 14(b) summarizes the number of bands on the domain as a function of H_0 from all of the trials for increasing H_0 (blue) and decreasing H_0 (red). We note that band merging and band splitting events were also observed in a study of the extended Klausmeier model when the annual mean precipitation was slowly ramped down and back up [46]. Those typically occurred as spatial period-doubling or period-halving in this simpler deterministic model setting. In the stochastic pulsed-precipitation model results shown in Figure 14 there is more variability in the band loss and gain events, which here occur without any changes in the mean annual precipitation.

We have made a number of simplifying assumptions in this work, particularly in the overland flow model, with the goal of allowing for analytic insight and computational efficiency. The form of the infiltration model neglects soil saturation effects, which may become important when considering very intense rainstorms. The choice of periodic boundary conditions does

not allow for exploration of the impact of surface water run off. Both effects have been considered in [8, 45] using very different approaches to model surface hydrology. We note that the work of Crompton and Thompson [8] indicates that storm duration plays an equally important role as storm depth in pattern formation, as both can affect rainfall intensity. Our assumption of instantaneous rain pulses does not allow us to explicitly explore the impact of storm duration, separate from storm depth, on pattern formation. The possibility that we might reinterpret our storm depth parameter, which determined pattern wavelength in our pulsed model, as capturing an effective surface water height during storms will be the subject of future work, in which storm duration is included in our model.

Our focus in this work has been on capturing the influence of hydrological processes across timescales, and the biomass model used here is based directly on previous conceptual models [21, 38]. Other works have explored the impacts of incorporating additional vegetation characteristics and processes [3, 4, 13, 15, 25, 36, 41]. Fortunately, as indicated in Appendix A, we did not find a strong dependence of simulation results on the biomass diffusion rate, which is a phenomenological parameter that is not well constrained by observation.

Generalizing the pulsed-precipitation framework to capture the influence of heterogeneous terrain and moving to two spatial dimensions would open the door to a number of possible future directions. For example, an investigation of the Klausmeier model [27] with topographically modified water transport suggested that the placement of patterns relative to local valleys and ridges may provide an indicator for resilience of the ecosystem to drought [20]. It would be interesting to explore what additional insights could be gained by a two-dimensional pulsed-precipitation model that captures the influence of various rainfall characteristics, not just the mean precipitation value that controls drought. Capturing hydrology on the fast timescale could also allow for the exploration of the impact of roads, noted, for example, in [23], or other disruptions to surface water flow on the vegetation patterns. It is also likely to be important when coupling to landscape evolution through erosion and sediment transport.

Theoretical studies have suggested that spatial patterns can increase ecosystem resilience and protect it against collapse under a decrease in total rainfall [32, 37]. However, climate change will impact not only the yearly mean rainfall. It is already seen to disrupt seasonality in rainfall patterns and increase variability in storm characteristics. A framework like the pulsed-precipitation model, which can capture the influence of changing rainfall patterns, may therefore be useful since it can assess resilience in those contexts. It also brings into sharp focus the driving role of the fast hydrological processes on the dynamics of dryland vegetation patterns, which then evolve on their own years-to-decades timescales. This highlights the potential for time-resolved data from field-based hydrology monitoring, across vegetation bands, as a welcome and timely feedback to mathematical modeling efforts.

Appendix A. Dependence of pattern formation on soil water and biomass diffusion rates. The soil water and biomass diffusion rates D_W and D_B are typically not well constrained by observation in reaction-diffusion models of vegetation pattern formation (see, e.g., [19]). This appendix explores the dependence of pattern formation on these constants in the pulsed-precipitation model with stochastic rain input. We take $\mathcal{MAP} = 16 \,\mathrm{cm}$, mean storm depth $H_0 = 1 \,\mathrm{cm}$, and $T_r \to 0$, as done in section 5.3. 500-year simulations with the same initial condition and rainfall sequence but different diffusion rates are carried out on a 1000-m

domain. The thumbnails of spacetime plots of biomass shown in Figure 15 illustrate the qualitative influence of D_B on the uphill migration rate of the pattern. We see relatively minor impact from changing D_W across three orders of magnitude. Importantly, selection of the pattern wavelength is insensitive to the values of *both* diffusion constants.

Appendix B. Comparison of pulsed-precipitation model to fast-slow model. This appendix provides a comparison of simulation results from the fast-slow model [18], described in section 2, to corresponding results from the pulsed-precipitation model, presented in section 3. Some care must be taken to make the comparison as the fast-slow model incorporates both storm depth and duration, whereas the pulsed-precipitation model assumes instantaneous rain impulses (with no duration). We can, however, account for this by interpreting the storm depth associated with an impulsive rain storm from the pulsed-precipitation model as an effective surface water height that is achieved during a storm of finite duration in the fast-slow model.

Figure 16 shows results from simulations of the fast-slow model using the same parameters as [18], which are also reported in section 2. A mean annual rainfall of $\mathcal{MAP} = 16\,\mathrm{cm}$ is used, and each of two identical rainy seasons per year is modeled by a single storm with constant rainfall rate P_0 of duration $T_{dur} = 45\,\mathrm{min}$, $90\,\mathrm{min}$, $3\,\mathrm{hrs}$, $6\,\mathrm{hrs}$, $12\,\mathrm{hrs}$, and $24\,\mathrm{hrs}$. Simulations with each of these six rainstorm durations are initialized with 1% random noise on top of a uniform vegetation state and run for 200 years. We take the peak surface water height achieved at each point on the $500\,\mathrm{m}$ domain during the final cycle of the fast system (i.e., the time period over which water from the last rainstorm of the simulation remains on the surface) and plot the spatial average of this profile (denoted by H) as a function of the rainfall rate during the storm in Figure 16(a).

This domain-averaged peak surface water height H, captured by Figure 16(a), provides a path to compare the fast-slow model to the pulsed-precipitation model. In particular, we interpret the mean storm depth parameter H_0 of the pulsed-precipitation model as an effective peak surface water height, analogous to the quantity H from the fast-slow model described above. Instead of taking H_0 as the total mean rainfall during storms, we can then think of it as characterizing an effective peak surface water height during storms that takes into account both the influence of storm depth and duration. We run 150 total trials of the stochastic pulsed-precipitation model, also with $\mathcal{MAP} = 16\,\mathrm{cm}$ and two rainy seasons per year on a 500-m domain initialized with 1% noise added to a uniform vegetation state. We do five trails at each mean storm depth value $0.2\,\mathrm{cm} \leq H_0 \leq 6\,\mathrm{cm}$ at $0.2\,\mathrm{cm}$ increments. For the last 20 years of each 200-year trial, we compute the mean storm depth during that year, the number of bands in the pattern, the domain-averaged peak biomass and soil water during the year, and the domain-averaged infiltration rate during the storm pulse. These are compared to the analogous quantities obtained with the fast-slow model in Figure 16(b).

In each of the four panels shown in Figure 16(b) the mean value of the quantity, as a function of mean storm depth from the stochastic pulsed-precipitation simulations, is plotted with a solid line. The interquartile range is shaded, and the minimum and maximum values obtained from the trials are also indicated by dotted lines. The black circles indicate values from the final year of the fast-slow simulation. We see agreement in the biomass and soil water levels between the two models. The number of bands is also consistent between the two models

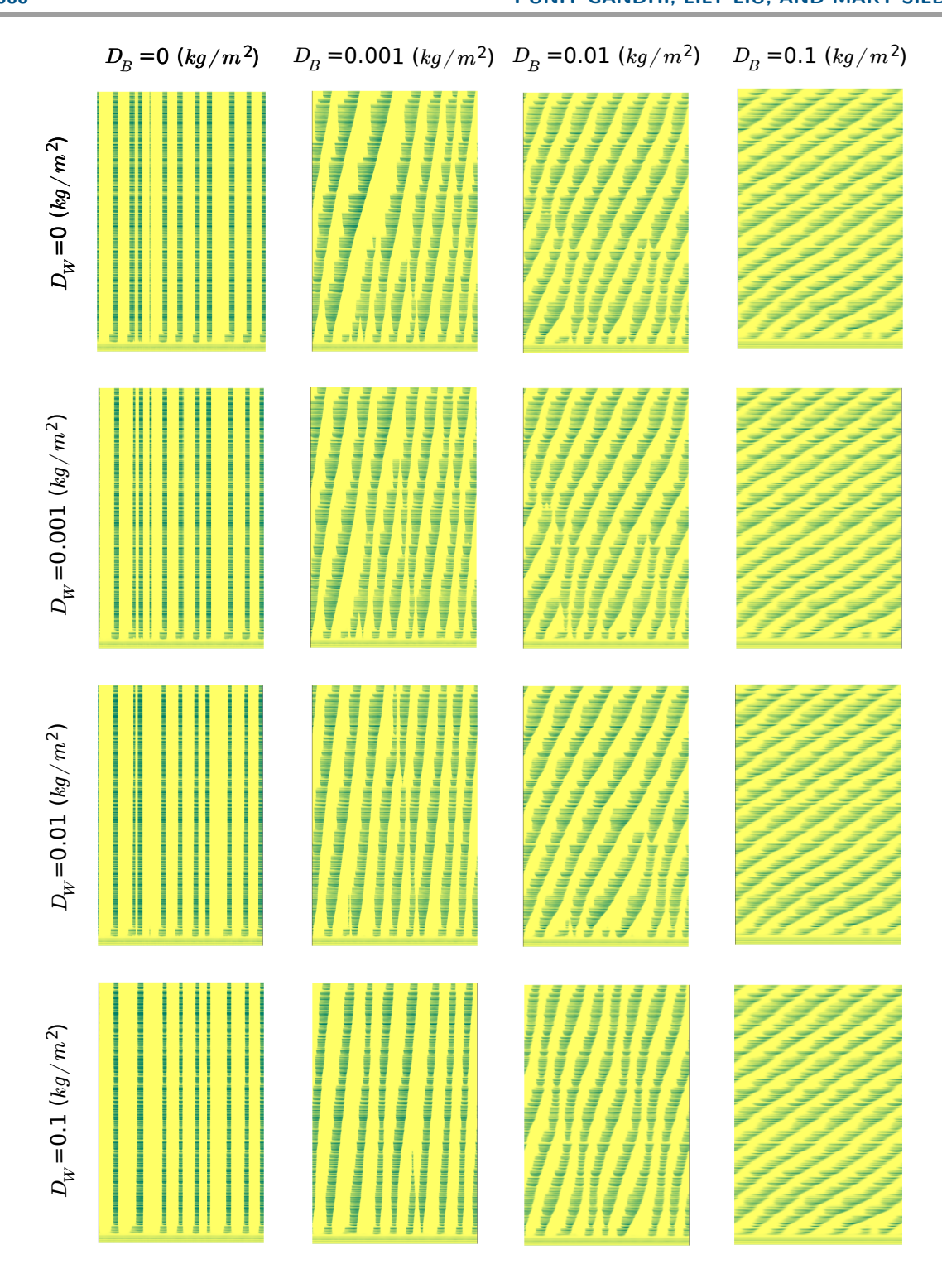


Figure 15. Dependence of pattern characteristics on biomass and soil water diffusion rates. Thumbnail plots of annually averaged biomass in units of kg/m² as a function of space (horizontal axis) and time (vertical axis) are shown for different biomass and soil water diffusion rates D_W , $D_B = 0$, 0.001, 0.01, and 0.1 kg/m². The color scale is the same as in Figures 6 and 8. Each simulation has the same stochastic rainfall sequence for a total of 500 years, with $\mathcal{MAP} = 16\,\mathrm{cm}$, mean storm depth $H_0 = 1\,\mathrm{cm}$, and rainy season duration $T_r \to 0$ on a $L = 1000\,\mathrm{m}$ domain, and is initialized with the same 1% random noise on top of the spatially uniform solution.

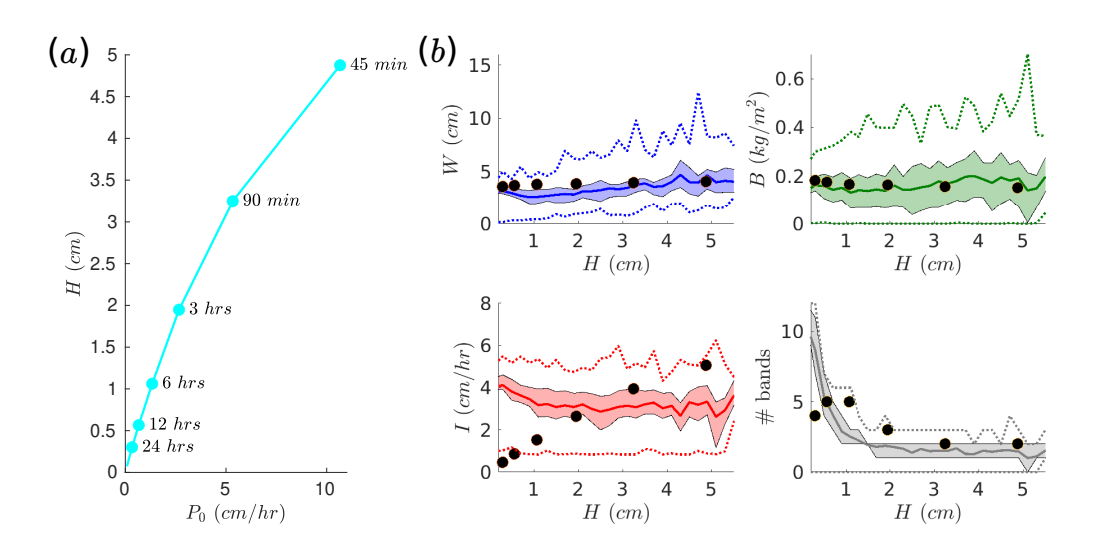


Figure 16. A comparison of the pulsed-precipitation model to the fast-slow model [18]. Simulations of the fast-slow model use a fixed mean annual precipitation $\mathcal{MAP}=16\,\mathrm{cm}$ over two equally spaced storms per year with durations $T_{dur}=45\,\mathrm{min}$ up to 24 hrs and are initialized with 1% noise on top of a uniform state and a domain of $L=500\,\mathrm{m}$. The results of 200-year simulations are compared to analogous results from 150 trials of the pulsed-precipitation model with different stochastic rainfall with mean storm depths from $H=0.2\,\mathrm{cm}$ up to 6 cm. (a) The domain-averaged, temporal-maximum surface water height from simulations of the fast-slow model during the storm is shown as a function of rainfall rate, and the points are labeled by the storm duration. (b) The domain-averaged soil water, biomass, infiltration rate, and number of bands from the final year of the fast-slow simulations, indicated by black circles, are compared to analogous results from the stochastic pulsed-precipitation model. In each case the mean value of the quantity as a function of the mean storm depth H is plotted with a thick solid line. The interquartile range is shaded, and the minimum/maximum values are indicated by dotted lines.

for larger H. At small H, the difference in the infiltration rate functions between the two models may explain the differences in the predicted band spacing. Indeed, we see improved agreement in both lower panels of Figure 16(b) in simulations (not shown) where we decrease the parameter A in the infiltration function of the fast-slow model below its default value $A = 1 \,\mathrm{cm}$. Specifically, we refer to the factor H/(H+A) in the fast-slow infiltration function given in Table 1; decreasing A makes the fast-slower infiltration closer to the step-function used in the pulsed-precipitation model. We note that Thompson et al. [47] have explored the dependence of the infiltration rate on surface water height in the context of so-called flat-terrain vegetation patterns.

Last, we emphasize that the computational savings of the pulsed-precipitation model over the fast-slow model are significant. We see a factor of 200 or more speedup in simulation time by going from the fast-slow model to the analogous pulsed-precipitation simulation in the comparisons presented here.

Appendix C. Linear stability of bare soil state to uniform perturbations. In this appendix we consider the linear stability of the zero biomass desert state to spatially uniform perturbations. (We need not consider heterogeneous perturbations, proportional to e^{ikx} , for

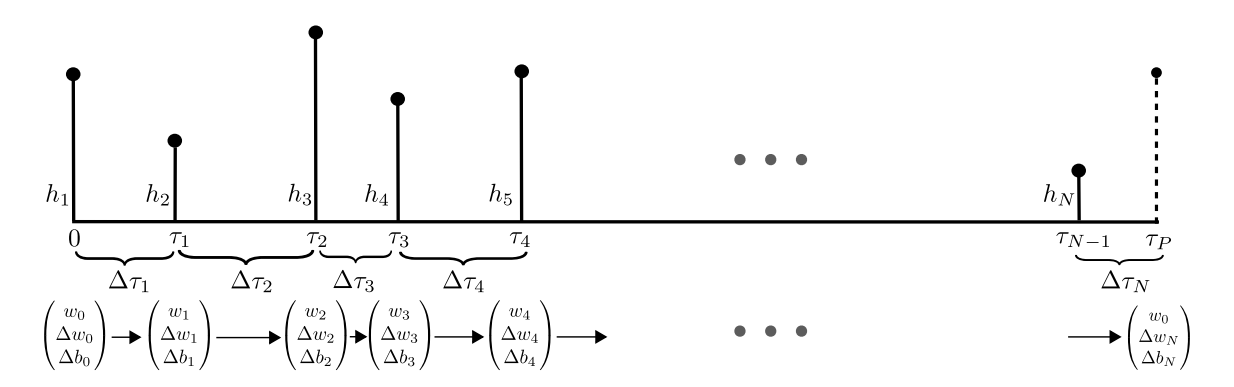


Figure 17. Summary of rainfall model and other quantities introduced for the linear stability analysis.

the zero biomass state since we require $b \ge 0$.) We show that the \mathcal{MAP} threshold for loss of stability, denoted by \mathcal{MAP}_c , is independent of details of the rainfall model. We consider N pulses of rain per year, with strengths h_k , k = 1, ..., N, which repeat annually and sum to \mathcal{MAP} . The temporal spacing between pulses is denoted by $\Delta \tau_k$, k = 1, ..., N, and these time intervals sum to $\tau_P = 3.65$, i.e., 1 year in dimensionless units. The periodic rainfall model and the parameters needed for the linear stability analysis are summarized in Figure 17.

The base state for the linear stability analysis has b=0 and a soil moisture level that repeats with the annual period. Let w_0 be the initial condition for this periodic base state, and denote the soil moisture at time τ_k , prior to the kth pulse of strength h_k , by w_k . From (4.3), we have that a pulse of strength h adds αh to w and, from (4.9a), that a dry period of duration $\Delta \tau$ leads to its evaporative decay by a factor $e^{-\sigma \Delta t}$. It follows that

(C.1)
$$w_{k+1} = (w_k + \alpha h_1)e^{-\sigma \Delta t_k}, \quad k = 0, \dots, N-1.$$

Moreover, we require $w_N = w_0$ for the periodic state, which determines w_0 .

We perturb this $(w,b) = (w(\tau),0)$ base state by $(\Delta w_0, \Delta b_0)$ at time $\tau = 0$. This perturbation advances to a value $(\Delta w_1, \Delta b_1)$ at time $\Delta \tau_1$, and so on. We obtain, for example, $(\Delta w_1, \Delta b_1)$ by evolving the following linearized slow system equations for time $\Delta \tau_1$:

$$\frac{d}{d\tau} \begin{pmatrix} \Delta w \\ \Delta b \end{pmatrix} = \begin{pmatrix} -\sigma & \gamma w(\tau) \\ 0 & w(\tau) - 1 \end{pmatrix} \begin{pmatrix} \Delta w \\ \Delta b \end{pmatrix},$$

where here $w(\tau) = (w_0 + \alpha h_1)e^{-\sigma\tau}$ for $\tau \in (0, \Delta \tau_1)$. From this, we obtain the following map:

$$\begin{pmatrix} \Delta w_1 \\ \Delta b_1 \end{pmatrix} = \begin{pmatrix} e^{-\sigma \Delta \tau_1} & * \\ 0 & e^{\chi_1} \end{pmatrix} \begin{pmatrix} \Delta w_0 \\ \Delta b_0 \end{pmatrix},$$

where the off-diagonal term * is not needed for determining stability, and

$$\chi_1 = \int_0^{\Delta \tau_1} (w(\tau) - 1) \ d\tau = \left(\frac{w_0 + \alpha h_1}{\sigma}\right) \left(1 - e^{-\sigma \Delta \tau_1}\right) - \Delta \tau_1 = \left(\frac{w_0 + \alpha h_1 - w_1}{\sigma}\right) - \Delta \tau.$$

Here the final equality follows from (C.1). Repeating this for the N rain pulses, we find

$$\begin{pmatrix} \Delta w_N \\ \Delta b_N \end{pmatrix} = \begin{pmatrix} e^{-\sigma \tau_P} & * \\ 0 & e^{\chi_1 + \chi_2 + \dots + \chi_N} \end{pmatrix} \begin{pmatrix} \Delta w_0 \\ \Delta b_0 \end{pmatrix},$$

where

$$\chi_k = \int_{\tau_{k-1}}^{\tau_k} (w(\tau) - 1) \ d\tau = \left(\frac{w_{k-1} + \alpha h_k - w_k}{\sigma}\right) - \Delta \tau_k.$$

The stability boundary, denoted by \mathcal{MAP}_c is determined by the condition $\chi_1 + \cdots + \chi_N = 0$. Using the fact that $w_0 = w_N$ and that $\Delta \tau_1 + \cdots + \Delta \tau_N = \tau_P$, it follows that

$$\mathcal{MAP}_c = h_1 + \dots + h_N = \frac{\sigma \tau_P}{\alpha},$$

which, in dimensioned quantities, is $(LM/C\Gamma)365 = 10.95 \,\mathrm{cm/yr}$ for the parameters of Table 2.

Acknowledgments. We would like to thank Merlin Pelz, Justin Finkel, Shiv Agrawal, Octavia Crompton, Karna Gowda, and Sarah Iams for helpful discussions related to this work. Computing resources were provided by the High Performance Research Computing (HPRC) Core Facility at Virginia Commonwealth University.

REFERENCES

- [1] R. Bastiaansen, A. Doelman, M. B. Eppinga, and M. Rietkerk, The effect of climate change on the resilience of ecosystems with adaptive spatial pattern formation, Ecol. Lett., 23 (2020), pp. 414–429.
- [2] R. Bastiaansen, O. Jaïbi, V. Deblauwe, M. B. Eppinga, K. Siteur, E. Siero, S. Mermoz, A. Bouvet, A. Doelman, and M. Rietkerk, Multistability of model and real dryland ecosystems through spatial self-organization, Proc. Natl. Acad. Sci. USA, 115 (2018), pp. 11256–11261.
- [3] J. J. R. Bennett and J. A. Sherratt, Long-distance seed dispersal affects the resilience of banded vegetation patterns in semi-deserts, J. Theoret. Biol., 481 (2019), pp. 151–161.
- [4] F. BORGOGNO, P. D'ODORICO, F. LAIO, AND L. RIDOLFI, Effect of rainfall interannual variability on the stability and resilience of dryland plant ecosystems, Water Resour. Res., 43 (2007).
- [5] F. BORGOGNO, P. D'ODORICO, F. LAIO, AND L. RIDOLFI, Mathematical models of vegetation pattern formation in ecohydrology, Rev. Geophys., 47 (2009).
- [6] A. CORNET, J.-P. DELHOUME, AND C. MONTANA, Dynamics of striped vegetation patterns and water balance in the Chihuahuan Desert, in Diversity and Pattern in Plant Communities, SPB Academic Publishing, The Hague, The Netherlands, 1988, pp. 221–231.
- [7] O. CROMPTON, G. G. KATUL, AND S. THOMPSON, Resistance formulations in shallow overland flow along a hillslope covered with patchy vegetation, Water Resour. Res., 56 (2020), e2020WR027194.
- [8] O. V. Crompton and S. E. Thompson, Sensitivity of dryland vegetation patterns to storm characteristics, Ecohydrology, 14 (2021), e2269.
- [9] V. Dakos, S. Kéfi, M. Rietkerk, E. H. Van Nes, and M. Scheffer, Slowing down in spatially patterned ecosystems at the brink of collapse, Am. Nat., 177 (2011), pp. E153–E166.
- [10] V. Deblauwe, N. Barbier, P. Couteron, O. Lejeune, and J. Bogaert, The global biogeography of semi-arid periodic vegetation patterns, Glob. Ecol. Biogeogr., 17 (2008), pp. 715–723.
- [11] V. Deblauwe, P. Couteron, J. Bogaert, and N. Barbier, Determinants and dynamics of banded vegetation pattern migration in arid climates, Ecol. Monogr., 82 (2012), pp. 3–21.
- [12] V. Deblauwe, P. Couteron, O. Lejeune, J. Bogaert, and N. Barbier, Environmental modulation of self-organized periodic vegetation patterns in Sudan, Ecography, 34 (2011), pp. 990–1001.

- [13] P. D'Odorico, F. Laio, and L. Ridolfi, Vegetation patterns induced by random climate fluctuations, Geophys. Res. Lett., 33 (2006).
- [14] M. DRUSCH, U. D. BELLO, S. CARLIER, O. COLIN, V. FERNANDEZ, F. GASCON, B. HOERSCH, C. ISOLA, P. LABERINTI, P. MARTIMORT, A. MEYGRET, F. SPOTO, O. SY, F. MARCHESE, AND P. BARGELLINI, Sentinel-2: ESA's optical high-resolution mission for GMES operational services, Remote Sens. Environ., 120 (2012), pp. 25–36, https://doi.org/10.1016/j.rse.2011.11.026.
- [15] L. EIGENTLER AND J. A. SHERRATT, Effects of precipitation intermittency on vegetation patterns in semi-arid landscapes, Phys. D, 405 (2020), 132396.
- [16] L. C. EVANS, Partial Differential Equations, 2nd ed., American Mathematical Society, Providence, RI, 2010.
- [17] S. FATICHI, V. Y. IVANOV, AND E. CAPORALI, A mechanistic ecohydrological model to investigate complex interactions in cold and warm water-controlled environments: 1. Theoretical framework and plot-scale analysis, J. Adv. Model. Earth Syst., 4 (2012).
- [18] P. GANDHI, S. BONETTI, S. IAMS, A. PORPORATO, AND M. SILBER, A fast-slow model of banded vegetation pattern formation in drylands, Phys. D, 410 (2020), 132534.
- [19] P. Gandhi, S. Iams, S. Bonetti, and M. Silber, Vegetation pattern formation in drylands, in Dryland Ecohydrology, Springer, Cham, 2019, pp. 469–509.
- [20] P. GANDHI, L. WERNER, S. IAMS, K. GOWDA, AND M. SILBER, A topographic mechanism for arcing of dryland vegetation bands, J. R. Soc. Interface, 15 (2018), 20180508.
- [21] E. GILAD, J. VON HARDENBERG, A. PROVENZALE, M. SHACHAK, AND E. MERON, Ecosystem engineers: From pattern formation to habitat creation, Phys. Rev. Lett., 93 (2004), 098105.
- [22] K. GOWDA, Y. CHEN, S. IAMS, AND M. SILBER, Assessing the robustness of spatial pattern sequences in a dryland vegetation model, Proc. A, 472 (2016), 20150893.
- [23] K. GOWDA, S. IAMS, AND M. SILBER, Signatures of human impact on self-organized vegetation in the Horn of Africa, Sci. Rep., 8 (2018), 3622.
- [24] K. GOWDA, H. RIECKE, AND M. SILBER, Transitions between patterned states in vegetation models for semiarid ecosystems, Phys. Rev. E (3), 89 (2014), 022701.
- [25] V. Guttal and C. Jayaprakash, Self-organization and productivity in semi-arid ecosystems: Implications of seasonality in rainfall, J. Theoret. Biol., 248 (2007), pp. 490–500.
- [26] G. J. Huffman, D. T. Bolvin, D. Braithwaite, K. Hsu, R. Joyce, P. Xie, and S.-H. Yoo, NASA global precipitation measurement (GPM) integrated multi-satellite retrievals for GPM (IMERG), in Algorithm Theoretical Basis Document (ATBD) Version 4, 2015, p. 26.
- [27] C. A. Klausmeier, Regular and irregular patterns in semiarid vegetation, Science, 284 (1999), pp. 1826–1828.
- [28] A. Y. Kletter, J. Von Hardenberg, E. Meron, and A. Provenzale, *Patterned vegetation and rainfall intermittency*, J. Theoret. Biol., 256 (2009), pp. 574–583.
- [29] M. A. Lewis and B. Li, Spreading speed, traveling waves, and minimal domain size in impulsive reactiondiffusion models, Bull. Math. Biol., 74 (2012), pp. 2383–2402.
- [30] W. A. MACFADYEN, Soil and vegetation in British Somaliland, Nature, 165 (1950), 121.
- [31] W. A. Macfadyen, Vegetation patterns in the semi-desert plains of British Somaliland, Geogr. J., 116 (1950), pp. 199–211.
- [32] Y. Mau, L. Haim, and E. Meron, Reversing desertification as a spatial resonance problem, Phys. Rev. E (3), 91 (2015), 012903.
- [33] E. Meron, Nonlinear Physics of Ecosystems, CRC Press, Boca Raton, FL, 2015.
- [34] K. MEYER, A. HOYER-LEITZEL, S. IAMS, I. KLASKY, V. LEE, S. LIGTENBERG, E. BUSSMANN, AND M. L. ZEEMAN, Quantifying resilience to recurrent ecosystem disturbances using flow-kick dynamics, Nat. Sustain., 1 (2018), pp. 671–678.
- [35] A. Paschalis, G. G. Katul, S. Fatichi, G. Manoli, and P. Molnar, *Matching ecohydrological processes and scales of banded vegetation patterns in semiarid catchments*, Water Resour. Res., 52 (2016), pp. 2259–2278.
- [36] Y. Pueyo, S. Kéfi, C. Alados, and M. Rietkerk, Dispersal strategies and spatial organization of vegetation in arid ecosystems, Oikos, 117 (2008), pp. 1522–1532.
- [37] M. RIETKERK, R. BASTIAANSEN, S. BANERJEE, J. VAN DE KOPPEL, M. BAUDENA, AND A. DOELMAN, Evasion of tipping in complex systems through spatial pattern formation, Science, 374 (2021), eabj0359.

- [38] M. RIETKERK, M. C. BOERLIJST, F. VAN LANGEVELDE, R. HILLERISLAMBERS, J. VAN DE KOPPEL, L. KUMAR, H. H. T. PRINS, AND A. M. DE ROOS, Self-organization of vegetation in arid ecosystems, Am. Nat., 160 (2002), pp. 524–530.
- [39] M. RIETKERK, S. C. DEKKER, P. C. DE RUITER, AND J. VAN DE KOPPEL, Self-organized patchiness and catastrophic shifts in ecosystems, Science, 305 (2004), pp. 1926–1929.
- [40] I. Rodriguez-Iturbe, A. Porporato, L. Ridolfi, V. Isham, and D. R. Coxi, Probabilistic modelling of water balance at a point: The role of climate, soil and vegetation, Proc. A, 455 (1999), pp. 3789–3805.
- [41] P. M. SACO, G. R. WILLGOOSE, AND G. R. HANCOCK, Eco-geomorphology of banded vegetation patterns in arid and semi-arid regions, Hydrol. Earth Syst. Sci., 11 (2007), pp. 1717–1730.
- [42] L. F.SHAMPINE AND M. W.REICHELT, The MATLAB ODE suite, SIAM J. Sci. Comput., 18 (1997), pp. 1–22, https://doi.org/10.1137/S1064827594276424.
- [43] J. A. Sherratt, An analysis of vegetation stripe formation in semi-arid landscapes, J. Math. Biol., 51 (2005), pp. 183–197.
- [44] E. SIERO, A. DOELMAN, M. EPPINGA, J. D. RADEMACHER, M. RIETKERK, AND K. SITEUR, Striped pattern selection by advective reaction-diffusion systems: Resilience of banded vegetation on slopes, Chaos, 25 (2015), 036411.
- [45] K. Siteur, M. B. Eppinga, D. Karssenberg, M. Baudena, M. F. P. Bierkens, and M. Rietkerk, How will increases in rainfall intensity affect semiarid ecosystems?, Water Resour. Res., 50 (2014), pp. 5980–6001.
- [46] K. Siteur, E. Siero, M. B. Eppinga, J. D. Rademacher, A. Doelman, and M. Rietkerk, Beyond Turing: The response of patterned ecosystems to environmental change, Ecol. Complex., 20 (2014), pp. 81–96.
- [47] S. E. THOMPSON, C. J. HARMAN, P. HEINE, AND G. G. KATUL, Vegetation-infiltration relationships across climatic and soil type gradients, J. Geophys. Res. Biogeosci., 115 (2010).
- [48] S. VAN DER STELT, A. DOELMAN, G. HEK, AND J. D. M. RADEMACHER, Rise and fall of periodic patterns for a generalized Klausmeier-Gray-Scott model, J. Nonlinear Sci., 23 (2013), pp. 39–95.
- [49] J. VON HARDENBERG, E. MERON, M. SHACHAK, AND Y. ZARMI, Diversity of vegetation patterns and desertification, Phys. Rev. Lett., 87 (2001), 198101.
- [50] C. M. Wainwright, J. H. Marsham, R. J. Keane, D. P. Rowell, D. L. Finney, E. Black, and R. P. Allan, "Eastern African paradox" rainfall decline due to shorter not less intense long rains, NPJ Clim. Atmos. Sci., 2 (2019), pp. 1–9.